The complex dynamics of gas percolation in low-porosity, crystal-rich silicic magmas

Anna Theurel, Marielle Collombet, Alain Burgisser, Caroline Martel, Laurent Arbaret, Rémi Champallier

Journal of Volcanology and Geothermal Research 474 (2026) 108612

Contents lists available at ScienceDirect

Journal of Volcanology and Geothermal Research

journal homepage: www.journals.elsevier.com/journal-of-volcanology-and-geothermal-research

The complex dynamics of gas percolation in low-porosity, crystal-rich silicic magmas

Anna Theurel [a,*], Marielle Collombet [b], Alain Burgisser [b], Caroline Martel [c], Laurent Arbaret [c], Rémi Champallier [c]

[a] Department of Earth Sciences, Durham University, Durham DH1 3LE, UK
[b] Univ. Savoie Mont Blanc, Univ. Grenoble Alpes, CNRS, IRD, Univ. Gustave Eiffel, ISTerre, 38000 Grenoble, France
[c] Institut des Sciences de la Terre d'Orléans (ISTO), University Orléans, CNRS, BRGM, Orléans, France

ARTICLE INFO

Keywords:
Magma permeability
Bubble dynamics
Outgassing
High-pressure high-temperature experiments

ABSTRACT

The dynamic of volcanic eruptions is closely linked to the style of degassing. The evidence of outgassing at the surface hints that gas dynamics can decouple from that of the magma. Constant outgassing, even during inter-eruptive periods, is at odds with our current understanding of the dynamics of highly viscous magmas, which precludes that mobile gas originating from deep within the conduit percolates through immobile magma. It has recently been suggested that permeability in crystal-rich, deep siliceous magma is made possible by extensive coalescence of bubbles, leading to channelling and, potentially, gas percolation at low porosity without external deformation. However, no temporal evolution of such permeability was suggested. Here, we present a time series of decompression experiments in internally heated pressure vessels using crystal-rich synthetic silicic magma samples. Documenting the early stages of coalescence to the near-final state of percolation, which sees the rupture of the permeable bubble chains, we propose a parameterization of the different processes involved in the bubble-by-bubble construction of the permeable networks up to the breakdown of these networks. Using our experimental results, we constrain inter-eruptive outgassing dynamics by considering theoretical eruptive scenarios to identify styles of deep magma degassing that could potentially be primers for future eruptions.

1. Introduction

Research on the behavior of silicic magma is essential to understand volcanic eruptions, both in terms of style (effusive-explosive) and intensity. In response to magma ascent, decompression of the conduit (dome collapse, fracture of the host rock, etc.), or concomitant crystallization of the magma, volatiles exsolve from the magma, leading to the nucleation and/or growth of gas bubbles. Studying the composition and quantity of volcanic gases enables us to constrain the origin of these gases at depth and on the related deep dynamics (e.g., Moussallam et al., 2017).

Surface outgassing is a well-documented process, both through field studies and experimental research. The presence of a large quantity of gas near the surface (due to lower pressure than at depth in the conduit, Jaupart and Allègre, 1991) generally implies high permeability of the magma (Klug and Cashman, 1996; Mueller et al., 2008, 2005). Deeper in the conduit, at pressures of a few to tens of MPa, experiments show that permeability can occur across a wide range of porosities, from 35 to 80 vol% bulk. In natural samples, primary permeability (i.e., solely due to coalescence of newly nucleated gas bubbles) is not always preserved, but it can exist in pumice clasts with as low as 30% porosity (Lindoo et al., 2016; Wright et al., 2009). The porosity above which permeability occurs is often called the critical porosity, or the percolation threshold. Numerical models suggest a relationship between crystal content and the critical porosity (Burgisser and Degruyter, 2015; Degruyter et al., 2019; Parmigiani et al., 2017). Gas percolation through a permeable magma may cause magma column outgassing, a process that has been studied through experiments, observations, and simulations. Previous studies (Daffos et al., 2025; Giachetti et al., 2019; Manga et al., 1998; Pistone et al., 2012) have shown that outgassing can also occur through deformation of bubbles during magma shearing or by buoyant rise of isolated bubbles if the magma viscosity is low enough. However, the porosity at which these various types of outgassing occur is often higher (>30%, deGraffenried et al., 2019; Graham et al., 2023; Lindoo et al., 2017, 2016; Mueller et al., 2005; Wright et al., 2009) than that typically found at depth in a conduit before an eruption (<10%, Collombet et al.,

* Corresponding author.
E-mail address: anna.theurel@durham.ac.uk (A. Theurel).

https://doi.org/10.1016/j.jvolgeores.2026.108612
Received 15 January 2026; Received in revised form 26 March 2026; Accepted 26 March 2026
Available online 27 March 2026

2021).

What is happening deep inside the conduit and in the chamber is more challenging to determine. At low porosity, in addition to fracture networks that allow high, secondary permeability (Heap and Kennedy, 2016), the primary phenomenon of gas channelling could enable gas to escape from the deep magma (Degruyter et al., 2019; Okumura et al., 2008). Despite these partial explanations, natural samples highlight a lack of understanding of deep outgassing processes. Indeed, during explosive eruptions, samples of magma from several kilometers below the surface (Wright et al., 2006b) can bear quantities of gas bubbles (i.e total porosity) well below those predicted by closed-system degassing (Burgisser et al., 2019; Collombet et al., 2021). These samples indicate that a significant quantity of gas had already been extracted from the magma at depth before the explosion.

A recent study (Theurel et al., 2024) provides experimental evidence of coalescence and channelling of gas bubbles in gas-poor, crystal-rich, and undeformed magma. Such conditions are a good proxy for deep, immobile magma. Although much attention has been given to the parameters controlling the effusive–explosive transition, the transition from inter-eruptive quiescence to eruptive activity is equally important because it is a simpler yet poorly understood situation. In other words, the mechanisms leading to permeability when the gas phase coexists with an immobile and highly viscous magma remain unclear. It is now essential to better constrain the time dependence of permeability from bubble growth to percolation. For this purpose, we have extended the study of Theurel et al., 2024, which consists of decompression experiments in internally heated pressure vessels (IHPV) followed by a dwell time of 1.5 h at final pressure, by varying the dwell time. We explore shorter (<3 min) and longer (2 days) dwell times to shed light on the dynamic evolution of permeability in a closed, immobile system. Finally, we propose scenarios of eruptive dynamics that highlight the implications of our findings.

2. Materials and methods

2.1. Sample composition

Our experimental set consists of two series that complement that presented in Theurel et al., 2024, which is labeled “series B" herein. The experimental magma is synthetic and three-phased. The liquid phase is a haplotonalite melt (HTN) representing a proxy of natural silica-rich melts (Supplementary Table S1) with a viscosity of around 10^4 Pa.s when hydrated with about 7 wt% H2O at 850 °C (Hess and Dingwell, 1996; Laumonier, 2013). The solid phase is composed of a well-constrained population of plagioclase microlites (most frequently measuring between 5 and 10 μm) with homogeneous shape and size distributions, that comes from the crystallization of HTN during the hydration phase before decompression (Mollard et al., 2012; Theurel et al., 2024). For some samples, equant-shaped alumina crystals of various sizes have been added: one population is ~50 μm in diameter to represent microphenocrysts, and the other is ~300 μm in diameter to represent phenocrysts. We will qualify, for simplicity, both alumina crystal sizes (50 and 300 μm) of phenocrysts.

The gas phase is made of distilled water, which saturates the melt during the high-pressure, high-temperature hydration phase and exsolves during decompression as supercritical water that we simply refer to as gas. We predicted the final gas content using the mass balance of Jaupart and Allègre (1991) constrained by our experimental conditions, i.e., the water content introduced in the capsule as initial water content, 120 MPa as final pressure, and a temperature of 850 °C.

Each series (A, B, and C) is composed of eight capsules. Two are only composed of HTN powder and water; two are composed of HTN powder, water, and 50 μm alumina crystals; two are composed of HTN powder, water, and 300 μm alumina crystals; and two are composed of HTN powder, water, and a mix of 50 μm and 300 μm alumina crystals. Plagioclase microlites are systematically crystallized in situ during the experiment. Each composition is sealed into gold capsules of 15 mm length, 5.4 mm outer diameter, and 0.2 mm thickness. The capsules are then checked visually and by weight difference before and after heating in an oven (150 °C) to ensure airtightness and prevent any leakage or contamination during the experiment.

2.2. Experimental techniques

The experimental procedure for both of our series is the same as that used by Theurel et al., 2024, which ensures a self-consistent time series. Experiments take place in an IHPV (Martel, 2012). Capsules are labeled and vertically oriented in a Kanthal furnace that is loaded in the IHPV and pressurized to 350 MPa using argon. Pressure is constantly monitored using a Heise Bourdon Gauge, ensuring 0.2 MPa precision. The temperature is also monitored continuously using two K-type thermocouples (precision of ±3 °C) under and above the capsules, allowing one to check that no temperature gradient occurs within the capsules. The samples are kept under 350 MPa and 850 °C overnight (at least 18 h) for hydration of the HTN glass powder and crystallization of plagioclase microlites. Following this hydration period, the samples are isothermally decompressed from 350 to 120 MPa in less than 4 min, i.e., a decompression rate of around 1 MPa/s, in order to expand gas bubbles. The experimental conditions are reported in supplementary material (Table 1).

Once decompressed, the two series have different dwelling times. Series A remains at 850 °C and 120 MPa for less than 1 min before isobaric quenching (5 min to glass transition), while series C remains under the same conditions for 48 h before undergoing the same type of quench. They can thus be compared with series B described in Theurel et al. (2024), which spent 1.5 h at 850 °C and 120 MPa (Table 1).

At the end of the experimental procedure, all capsules are examined individually to ensure that no leak occurred. Of all the capsules, only one from series A (sample A5) was found to be swollen when extracted from the autoclave and was thus discarded from the analyses on suspicion of puncture. All the remaining synthetic magma samples were carefully extracted from their gold capsules and subjected to various analyses.

2.3. Analytical methods

Every sample was scanned using a Phoenix Nanotom 180 X-ray

Table 1
Experimental conditions (850 °C, initial pressure P_{ini}). $Time_1$ is the saturation time, $Time_2$ is the decompression timescale and $Time_3$ is the dwelling time at final pressure (P_{final}).

Series	P_{ini} (MPa)	$Time_1$ (h)	Decompression			$Time_3$ (h)
			P_{final} (MPa)	$Time_2$ (s)	Rate (MPa/s)	
A	350	18	120	200	1.1	0.05
B*	350	18	120	180	1.3	1.5
C	350	18	120	150	1.5	48

* from Theurel et al. (2024).

computed microtomograph (μCT; ISTO) with a molybdenum target, a tungsten filament, an operating voltage of 94 kV and a filament current of 26 nA. Samples were rotated over 360° during the exposure to the X-radiation to obtain a complete 3D volume reconstructed using in-house Phoenix software. The average resolution of the volumes is 3 μm/voxel edge length. This resolution enables the visualization of the alumina crystals and the majority of the bubble population. However, this method is based on the density differences between the different objects observed, and the density of the HTN glass and the plagioclase microlites are very similar. In addition, the size of microlites is generally smaller than the resolution of tomography images. As a result, the microlites could not be observed or quantified using our μCT system, whereas it may be possible with a more powerful, synchrotron-based μCT.

The 3D μCT volumes are processed individually with FiJi/ImageJ software. Thanks to pixel gray-scale segmentation modules, the various phases are isolated from each other: gas bubbles in black, HTN melt mixture and plagioclase microlites in intermediate gray, and alumina crystals in light gray/white. This analysis allowed us to calculate the volume percentage of alumina crystals and to quantify various properties of the gas involved in the channelization process. The segmented volume of the gas phase is used to visualize and quantify bubble texture, bubble number density, bubble connectivity, bubble thickness (the diameter of the largest sphere that could fit in any given gas voxel) and, if so, the presence of permeable chains across the largest sub-volume containing only sample material. The latter is characterized by a continuous chain of connected white voxels (gas phase) across the volume that links two opposed faces of the volume. In such case, we consider this chain of bubbles/voxels as responsible for the percolation of gas through the sample. When sub-volumes are percolating, the permeability value is calculated in all directions of the sub-volume (340^3–600^3 voxels) using Lattice-Boltzmann fluid simulations with the Palabos software as described in Burgisser et al. (2019). The permeability of the alumina crystal network (Bretagne et al., 2023), usually called intrinsic permeability (Parmigiani et al., 2017), was measured in the same fashion by using volumes where only the alumina phase was segmented. Sub-volumes (a representative smaller sub-volume was used when necessary to keep the number of manually separated object within the software limit) of 7 samples were processed using the software Blob3D (Ketcham, 2005) to separate bubbles either by erosion or planar cut. Blob3D also calculated the longest axis of the ellipsoid fitted to the bubbles contained in the original sub-volumes to characterize the span of the interconnected bubble clusters.

After all samples have been scanned with μCT, they are divided into large fragments. Some fragments are placed on a resin pad, polished, and metalized for inspection by Scanning Electron Microscopy (SEM) with a JEOL JSM-6400 microscope operating at 15 to 20 kV accelerating voltages (ISTO). The resolution of our SEM images ranges from 0.01 to 1.5 μm/pixel. Using a cut-off value of 16 pixels (Giachetti et al., 2010), this method provides a visualization and a precise constraint on the size and quantity of microlites present in the melt, on the smallest bubbles in samples down to ~1 μm in diameter, and on the various characteristics of the bubbles. Given that SEM images are providing 2D information on a 3D network of interconnected objects, the shape of which differs significantly from a sphere (easily assessed in 2D), the merging of 2D SEM-based quantities with 3D μCT-based quantities is not trivial (this is discussed further in the Result section and the associated Fig. 9). Following the reasoning of Giachetti et al. (2010), we used two stereological methods to convert 2D size distributions into 3D distributions. The first method is that of Cheng and Lemlich (1983), which does not assume a specific object shape but does not correct for the cut effect (overestimation of small 2D objects that are in fact slices of larger 3D objects). The second method is that of Sahagian and Proussevitch (1998), which corrects for the cut effect by assuming a specific object shape. As there is no simple descriptor of the shape of interconnected bubbles at various stages of coalescence, we assumed a spherical shape for that method. We selected 8 samples to characterize the smallest bubble populations. As total bubble number densities are controlled by the number of small bubbles, we calculated them using the SEM distributions converted into 3D by the two stereological methods. As both methods yield similar number densities (difference of at most 0.1 log unit), we used only the distributions converted with the Cheng and Lemlich (1983) method to merge 6 of the 8 samples with their respective μCT distributions. The merging assumed that the number of objects between 10 and 20 μm equivalent diameter per volume unit, N, were the same in both distributions and using a 15 μm cut-off size between the two distributions (i.e. the number of bubble in each μCT bin was multiplied by the ratio of $N_{SEM}/N_{\mu CT}$). This merging method is equivalent to that of Giachetti et al. (2010) but with 3D distributions instead of 2D distributions.

We also performed statistical analysis on microlite orientations near bubbles in SEM images. We analyzed 105 bubble-microlite configurations on 15 samples coming from the three series. We used the SPO 2003 software (Launeau, 2004), which allows the user to determine the Shape Preferred Orientation of the crystals and to quantify crystal fabrics.

3. Results

Table 2 lists the physical characteristics of the samples after IHPV experiments. The SEM- and μCT-based gas phase quantification differ widely (Fig. S1A in the Supplementary Materials). This is mostly due to the small area covered by SEM images, which introduces inter-image variability within the same sample. The SEM magnification used to image our sample varies across images and ranges from 150× for a general visualization of the sample, to 1500× to constrain smallest features. This variability, which is generally biased toward large gas content because of the large size of the phenocrysts, can be illustrated by two SEM images taken on the same sample, yielding respectively 5.6 and 10.2 vol% of gas instead of the 3.5 vol% measured by μCT (Supplementary Material Fig. S1 A). We report in Table 2 the data stemming from the μCT volumes for two connected reasons. SEM images have higher resolution that captures well smaller objects such as microlites or small bubbles. Conversely, they misrepresent larger objects such as alumina crystals or larger bubbles, which are best captured by μCT volumes. The first reason to choose μCT data is thus that most of the volume fraction of the phases of interest is contained in large objects. The second reason is that, as a consequence, the predicted gas content (Table 2) matches the μCT data much better than the SEM data (Supplementary Material Fig. S1B and C).

Fig. 1 shows the bulk crystal and gas content of all samples obtained from the μCT volumes. The experimental procedure was designed to create time series where successive samples (Ax, Bx, and Cx with x = 1–8) represent progressively larger dwell times at final pressure in closed system. Fig. 1A shows that the series with x = 3, 4, 5, and 7 have respective gas and crystal contents that are similar within the measurement error. The small variability introduced by sample preparation (such as a typical ±0.1 wt% variability in capsule H_2O content) translates into a variable final gas content. As a result, series x = 1, 2, 6, and 8 have more variability and thus had close but not equal initial conditions (Fig. 1B).

3.1. Sample texture

3.1.1. Crystals

Two mineral compositions can be found in our samples (Table 2): plagioclase microlites and alumina (micro)phenocrysts. We first describe the plagioclases, which represent, on average, 53 ± 5 vol% of the microlite–melt mixture in all our samples. The shape of the plagioclases is tabular, typically with a shape ratio of 1:10:10 (Morgan and Jerram, 2006). This shape can be seen particularly well on the walls of gas bubbles in SEM images, which enable their 3D characterization. In our 2D SEM images, we mainly observe fine rods with a ratio of 1:10 because of the cut effect. The microlites present an automorphic shape

Table 2
Description of the samples after decompression experiments and isobaric quench.

		Crystals[a]				Gas bubbles[b]								Melt [c]	Sub-volume[d]
Series	N°	Size (μm)	Φ_{Al} vol % [a1]	Φ_{Plag} vol % [a2]	$\Phi_{Al+Plag}$ vol % [a3]	Φ_{Gas} vol % [b1]	$\Phi_{Gas}c$ vol % [b2]	Φ_{Gas} vol $\%_{melt}$ [b3]	logBND m^{-3} [b4]	log K_g [b5]	Connected porosity $vol\%_{melt}$ [b6]	Connected Porosity vol%rel	Biggest bubble vol%rel [b7]	Φ_{Melt} vol%	Size of sub-volume mm^3
A	1	10 + 50	50.7	21.5	72.2	8.7	6.9	31.4	13.6	–	–	–	–	19.1	3.1
	2	10 + 300	37.8	29.9	67.7	2.0	7.5	18.0	12.7	–	–	–	–	26.5	6.5
	3	10 + 50 + 300	52.8	19.9	72.7	9.6	6.8	35.2	13.1	−12.7 ***	18.4	10.7	9.7	17.7	6.8
	4	10	–	44.2	44.2	16.6	13.8	29.7	13.7	–	–	–	–	39.2	1.2
	5	10 + 50	n.a.[e]	n.a.	n.a.	n.a.	n.a.	n.a.	n.a.	n.a.	n.a.	n.a.	n.a.	n.a.	n.a
	6	10 + 300	50.1	23.0	73.1	3.5	6.3	23.8	12.7	–	–	–	–	20.5	3.8
	7	10 + 50 + 300	51.4	22.8	74.2	5.4	6.4	21.2	13.8	–	–	–	–	20.4	4.6
	8	10	–	46.6	46.6	12.0	13.2	22.5	13.7	–	–	–	–	41.4	1.9
B[‡]	**1**	10 + 50	50.1	21.2	71.3	9.8	7.1	34.3	13.4	−13.9 **	10.1	29.4	29.4	18.9	3.8
	2	10 + 300	44.8	25.4	70.2	7.1	7.4	24.1	12.4	−14.0 *	5.2	21.7	21.7	22.7	5.2
	3	10 + 50 + 300	37.9	28.4	66.3	8.5	8.3	25.2	13.3	−13.8 *	2.3	12.9	9.1	25.2	2.5
	4	10	–	45.3	45.3	14.5	13.6	26.6	13.5	–	–	–	–	40.2	0.8
	5	10 + 50	48.7	22.0	70.7	9.7	7.2	33.1	13.3	−13.9 *	7.8	23.5	23.5	19.6	3.5
	6	10 + 300	41.1	27.7	68.8	6.5	7.7	20.1	12.4	–	–	–	–	24.7	4.1
	7	10 + 50 + 300	50.6	22.7	73.3	6.4	6.6	24.1	13.3	–	–	–	–	20.3	1.8
	8	10	–	45.0	45.0	15.0	13.6	27.4	13.6	–	–	–	–	40.0	1.4
C	1	10 + 50	49.2	20.5	69.7	12.2	7.5	40.2	12.8	–	–	–	–	18.1	2.6
	2	10 + 300	47.7	22.7	70.4	9.5	7.4	32.0	12.0	–	–	–	–	20.1	4.4
	3	10 + 50 + 300	51.5	20.7	72.2	9.5	6.9	34.0	13.0	–	–	–	–	18.3	4.0
	4	10	–	45.1	45.1	14.9	13.6	27.1	13.1	–	–	–	–	40.0	1.4
	5	10 + 50	48.1	22.6	70.7	9.2	7.3	31.4	13.3	−13.8 *	3.1	10.0	10.0	20.1	3.0
	6	10 + 300	42.9	26.9	69.8	6.3	7.5	20.8	12.4	–	–	–	–	23.9	1.8
	7	10 + 50 + 300	49.0	24.0	73.0	5.8	6.7	21.5	13.5	–	–	–	–	21.2	4.8
	8	10	–	46.7	46.7	11.9	13.2	22.3	13.6	–	–	–	–	41.4	1.4

[a] Crystals consist of plagioclase microlites (Plag) and alumina microphenocrysts and phenocrysts (Al) (see 2.1).
[a1] [a2] Φ_{Plag} is the content of Plag (relative uncertainties of 3.0%) measured on SEM pictures and Φ_{Al} the content of Al (relative uncertainties of 8.9%) measured on μCT, calculated on a bulk (bubble-bearing) basis.
[a3] $\Phi_{Al+Plag}$ combines Φ_{Plag} and Φ_{Al}.
[b] Gas bubbles stand for the gas phase, whether it is isolated bubbles or sample-long chain of connected bubbles.
[b1] Φ_{gas} is the bulk gas content with relative uncertainties of 5.4% (phenocrysts present) and 2.6% (no phenocrysts), measured by compiling SEM and μCT data.
[b2] $\Phi_{gas}c$ is the predicted bulk gas content according to Jaupart and Allègre (1991) (relative uncertainties of 13%) (see 2.1).
[b3] Φ_{gas}melt is Φ_{gas} recalculated on the melt phase.
[b4] BND is the Bubble Number Density with respect to melt (absolute uncertainties of 0.1 log unit), measured by compiling SEM and μCT data.
[b5] K_g is gas permeability (absolute uncertainties of 0.3 log unit) (measured on μCT, see 3.3.1). The number of * describes the number of directions in which the sample is permeable.
[b6] Connected porosity of the sample is the proportion of gas percolating that allows gas permeability, measured on μCT.
[b7] The biggest bubble volume is the volume of the largest bubble in the sample, measured on μCT. It does not imply that the sample is permeable nor that the biggest bubble is responsible for the permeability (as for B3).
[c] The bulk melt content (Φ_{melt}) is the difference to 100% of the bulk contents of crystals and bubbles (100-$\Phi_{Plag+Al}$-Φ_{gas}).
[d] The sub-volume column represents the largest cuboid volume containing only sample material that can be cropped from the full μCT volume that contains the irregularly-shaped sample. These sub-volumes are used hereafter for all 3D quantifications and analyses.
[e] n.a. stand for not analyzed. The capsule containing sample A5 was found to be swollen after experiment, which is usually caused by capsule leakage. This sample was left out of the analysis.
[‡] Series B is from Theurel et al. (2024).

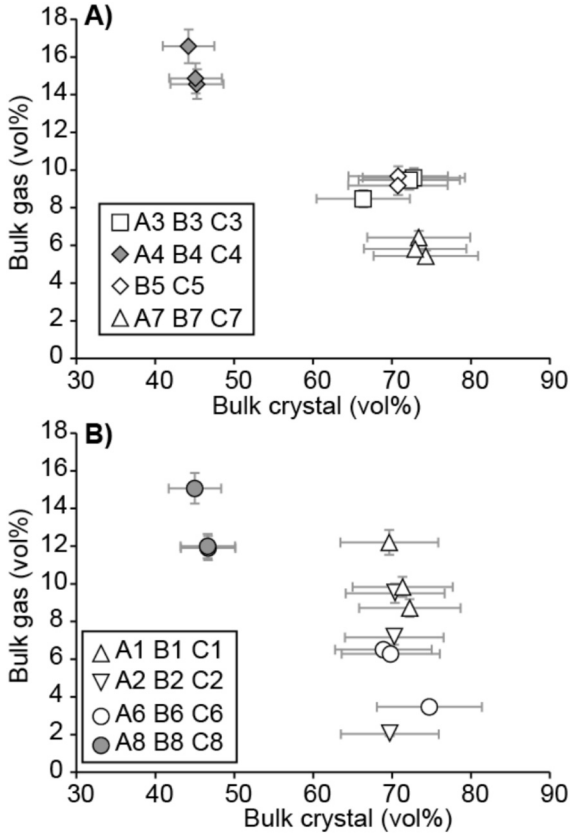

Fig. 1. Bulk gas content, Φ_{gas}, as a function of bulk crystal content,$\Phi_{Al+Plag}$. Errors smaller than the symbols are not shown. Samples are grouped by time series. A) Samples with matching gas and crystal content. B) Samples showing variability in gas and crystal content. Each symbol represents one composition (identified by the number) for the 3 different dwell times (identified by the letter, i.e., series A, B and C). Gray symbols represent alumina-free samples.

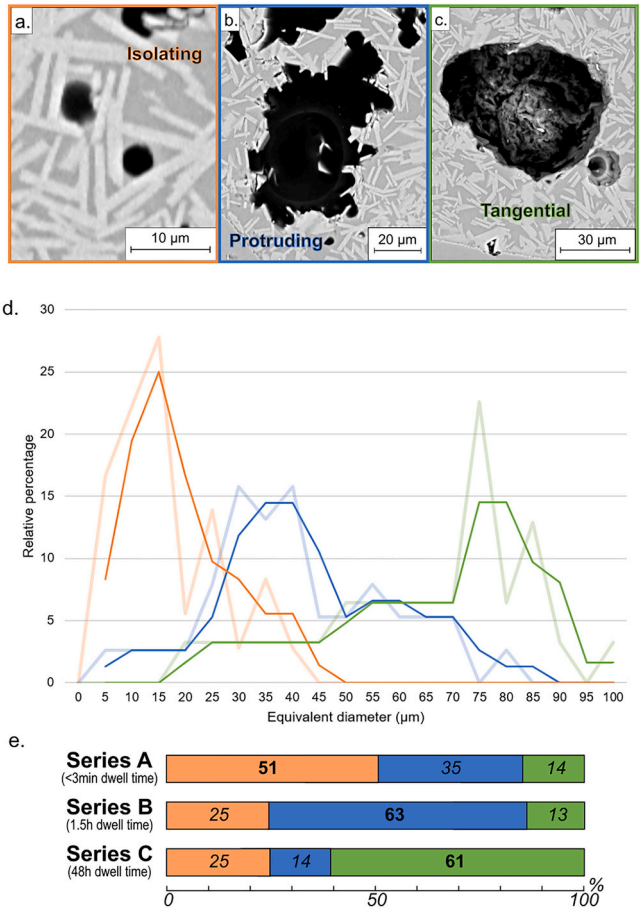

Fig. 2. Top: SEM images of a. Microlites isolating gas bubbles, b. Microlite protruding into a gas bubble, c. Microlites surrounding tangentially a gas bubble with smooth, low-curvature walls, d. relative percentage of bubbles showing isolating, protruding, or tangential style (curves from left to right, respectively) depending on their equivalent diameter size. Light curves are bulk data; plain curves are running averages with a sampling window of two values, e. proportion of number of bubbles from series A, B and C being surrounded by isolating, protruding, and tangential microlite types. See also Supplementary material Fig. S3 for more SEM example images.

with regular and straight sides (Fig. 2), suggesting that microlite crystallization achieved equilibrium. No growth aureoles were observed, nor were there any particular anomalies in their texture. Their size ranges from 1 to 20 µm in length, with an average monodisperse distribution around 5–7 µm (Supplementary Material from Theurel et al., 2024). As plagioclase crystals grow during the hydration phase before decompression, they have no dynamic influence on H_2O diffusion in the melt or on bubble growth; i.e. these processes do not happen simultaneously, therefore water diffusion and bubble growth occur in a stable crystallized material.

The shape preferred orientation of these plagioclase microlites is of interest. In our samples, we aimed at distinguishing fabrics at the global (thin section) scale, such as the possible presence of preferential orientation of microlites, from local fabrics, such as the orientation of microlites in contact with a bubble wall. The results of this analysis indicate that there is no global microlite fabric, confirming that the nucleation and growth of these crystals occurred homogeneously and at equilibrium (Supplementary Material Fig. S2).

At the local scale, three broad categories of microlite orientation with respect to the bubble surface can be observed. We recorded the size of bubbles from SEM images across all our samples as a function of these three categories and found that they depend on bubble size (Fig. 2). When bubbles are small (around 15 µm in equivalent diameter), the surrounding microlites seem to isolate the individual bubbles, often siding them (Fig. 2A). The relative bubble size distribution in Fig. 2D (orange curve) shows that a majority of smaller bubbles (<20 µm equivalent diameter) are surrounded by microlites, which are isolating them from other bubbles. In other words, either bubble growth has been limited by the presence of these randomly distributed crystals or the crystals have been displaced during bubble growth and aligned with the bubble surface. The latter case would imply that the melt viscosity during bubble growth is such that the crystals can move solely under the effect of gas expansion and thus without external constraints. These bubbles being surrounded by microlites are mainly present in series A (>50% of the bubbles, Fig. 2E).

Bubbles between 20 and 60 µm equivalent diameter (Fig. 2D, blue curve) have surrounding microlites organized very differently. Instead of being tangent to bubble walls, siding them, crystals protrude into the bubbles, often perpendicularly to the wall (Fig. 2B). This phenomenon is mainly observed in series B (Fig. 2E), where 63% of bubbles are surrounded by protruding microlites.

Finally, for the largest bubbles (generally larger than 70 µm equivalent diameter, Fig. 2D, green curve), microlites seem to have no impact on the shape of the bubbles, which are generally more spherical (Fig. 2C). In this case, microlites are neither isolating nor protruding. They are mainly oriented tangentially to the bubble walls, which confer a low curvature and smooth appearance to these walls. Although having orientations similar to those isolating smaller bubbles, tangential microlites are no longer a limiting parameter for bubble growth. In other words, isolating microlite act as a cage for the comparatively small growing bubble and prevents its evolution. Tangential microlites instead

surround bubbles that are comparatively so large that any additional bubble growth would affect microlite arrangement (i.e. the effective medium in which these large bubbles are suspended is composed of both microlites and melt). This tangential microlite category is dominant at long dwell times, occurring around more than 60% of the bubbles of series C (Fig. 2E).

The second mineral consists of alumina crystals. As listed in Table 2, six of the eight samples per series contain alumina crystals of various sizes. Using both 2D and 3D textural analyses, we determined a general homogeneity of the samples. Alumina crystals are chemically stable throughout the experiment and do not exhibit any variation of their shape and size. These crystals are homogeneously distributed in the volume and their presence does not affect the global homogeneous distribution of microlites in the melt. SEM images show, however, local heterogeneities around the edges of alumina crystals, which are generally surrounded by more densely packed plagioclase microlites. As a result, bubbles can only very rarely be found in direct contact with alumina crystals and are therefore not directly influenced by them. As dwelling times increase, the different bubble populations deform and coalesce in various ways (as described in the next Section). Nevertheless, the homogeneity of the alumina crystals remains, with no concentration gradient along the gravity direction, regardless of dwelling time or of ongoing bubble deformation and coalescence. Therefore, we assume that alumina crystals are immobile in all series, i.e., their arrangement in the magma seems independent of bubble proximity (regardless of bubble size) and of dwelling time.

3.1.2. Bubbles

In every sample, we observed several families of bubble sizes and textures, from isolated bubbles to percolating bubble chains, that are present in different proportions in the three dwelling times. These families were defined based on observed systematic variation of bubble number or gas volume as a function of the bubbles size range, but, as explained below, the cut-off values delimiting them were set somewhat arbitrarily as textural variations occur along a continuum. In our series, some samples are permeable to gas and certain bubble characteristics seem to be correlated with the presence of permeable pathways. In this section, we describe the characteristics of bubbles, linking them when relevant to the permeable/impermeable nature of the samples. The properties of the permeable networks are described in Section 3.3. The term of permeable chains/networks hereafter refer to continuous chain of extensively coalesced bubbles connecting two opposite faces of a given sub-volume.

The β class corresponds to bubbles between ~1 and 7 μm in size. The low-end cut-off value depends on the SEM resolution and varies from 1 to 1.9 μm. The high-end value corresponds to the average microlite length of 5–7 μm and below that value μCT data is noisy. As a result these bubbles are visible on μCT images but are more precisely constrained by SEM images (Fig. 3). This class represents between 0.2 and 2% of gas volume and are present consistently in every sample. Some of these bubbles were nucleated either during the hydration phase when plagioclase formed or during the decompression from 350 MPa to the final pressure of 120 MPa. They thus contain water. Others are composed by inert gas (Ar) trapped between the melt powder particles

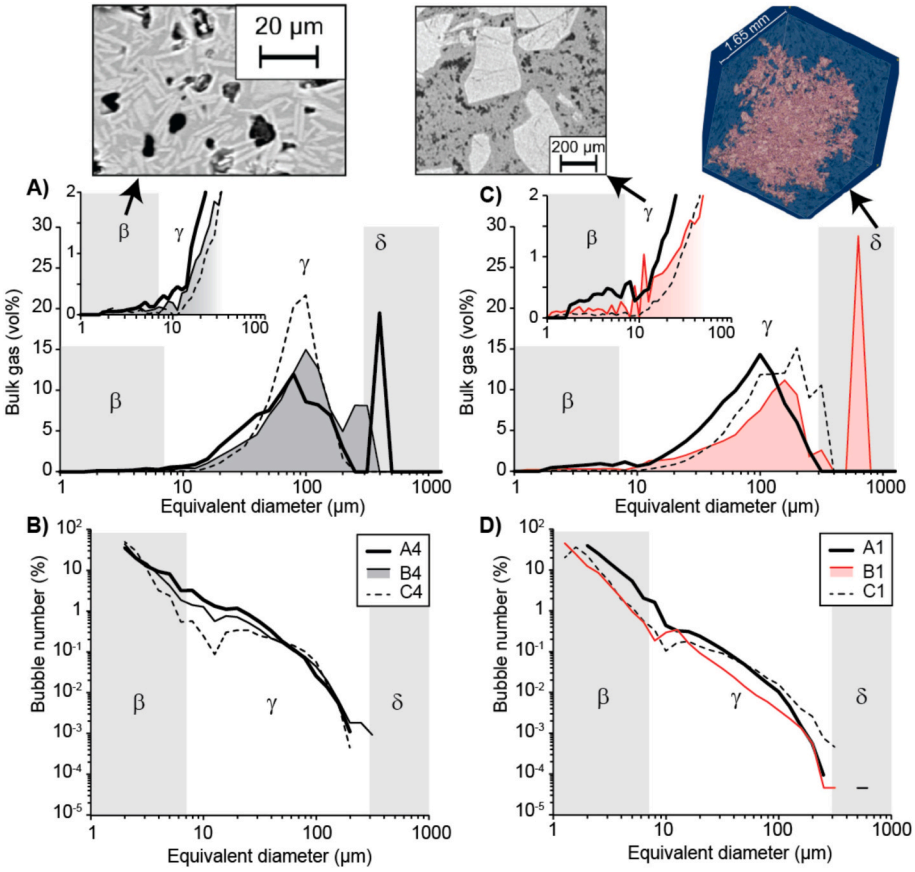

Fig. 3. Bubble size distributions of two representative time series obtained by merging SEM and μCT data. The ranges of textural classes β, γ, and δ are indicated on each graph. All samples are impermeable except B1 (in red). A) Distribution of gas volume fraction of series A4-B4-C4 (without alumina). B) Distribution of bubble number fraction of series A4-B4-C4. C) Distribution of gas volume fraction of series A1-B1-C1 (with alumina). D) Distribution of bubble number fraction of series A1-B1-C1. Class β is illustrated by a SEM image of A2. Class γ is illustrated by a raw (before any phase segmentation) μCT image of B2. Class δ is illustrated by a reconstructed 3D volume of the permeable sample B1 that highlights the largest percolating bubble. These samples are representative of the bubble populations found in the three series. Additional data on bubble size distributions can be found in Supplementary material 2 and in Supplementary material Video 1).

when melting, which do not contribute to any phenomena described in this study. We did not attempt to distinguish these various origins.

The γ class of bubbles appears to be the most sensitive to coalescence. It comprises bubbles between 7 and 300 μm equivalent diameter that show clearly defined peaks in volume proportion (Fig. 3A and C). The cut-off of 300 μm broadly corresponds to a trough in the distributions (Supplementary Material Figs. S4 and S5) but its value varies from sample to sample as an equivalent diameter only partly characterizes large bubbles clusters. This class spans the largest range of bubble sizes because it gathers all the intermediate size chains from the first chains made out of a couple of bubbles up to developed chains involving hundreds of initial bubbles.

Lastly, the δ class is characterized by the largest bubbles (greater than 300 μm equivalent diameter), which are generally composed of percolating (Fig. 3C, sample B1) or near-percolating (Fig. 3A, sample A4) bubble chains. As a result, this class is mainly present in permeable samples. It rarely contains more than ten bubbles but can account for up to 95% of the total gas volume.

Most bubbles of series A and B are far from spherical. Fig. 4 shows bubble thickness as a function of bubble volume. The thickness is a local measure of the bubble chains, and here we report density plots based on the median thickness of each bubble. In other words, a dendritic bubble cluster shape such as that illustrated in the 3D rendering in Fig. 3 is composed of interconnected bubbles forming chains of varying thicknesses. The median thickness of such a cluster gives a measure of the median size of the bubbles composing the chains. Fig. 4 shows that clusters of the series A and B are composed of chains that are mostly <15 μm thick. Series C, on the other hand, shows clusters that are closer to spherical with thicknesses reaching 25–35 μm.

Bubbles in our samples are sensitive to dwelling time, as illustrated in Fig. 3. The number of β class bubbles decreases slightly as dwelling time increases from <3 min. to 1.5 h (Fig. 3), which is mainly due to coalescence to form larger bubble belonging in γ- or δ-class bubbles. Similarly, bubbles isolated by surrounding microlites are less and less present with increased dwelling time (Fig. 2D and E). We, therefore, find many small bubbles for short dwelling times (Series A) and fewer large bubbles for long dwelling times (in Fig. 2D and E, the larger bubbles are usually surrounded by tangential microlites, and they are mainly present in Series C) despite having a similar total gas volume (Fig. 1). Bubble shapes also change with dwelling time. The 2D SEM images of Fig. 5 show that longer dwelling times produce more circular bubbles. Fig. 5 also shows that this trend is clear in samples without alumina crystals.

As suggested by the results of Fig. 4, bubble clusters are made of smaller bubbles, the size distribution of which is of interest to understand cluster genesis. Fig. 6 shows a selection of bubble size distributions from segmented μCT sub-volumes alongside the distribution obtained by de-coalescing bubble clusters (i.e. separating them by erosion/planar cuts into parent bubbles based on the constrictions indicating partially retracted bubble walls). To help visualize the typical bubble sizes involved in the coalescence process, Fig. 6 shows only the de-coalesced bubbles that were not in contact with the sub-volume sides. The original distributions include bubbles intersecting the sub-volume sides, and they are restricted to the range 7–300 μm (i.e. γ class) owing to the μCT resolution (3^3 μm^3 voxels) and the small size of the sub-volumes (rectangular cuboids of 0.3–0.8 mm^3) that yield sometimes large values of connected porosity. At short dwelling time (<3 min, Fig. 6A), very few large, ~80 μm clusters are present and they yield bubbles in the 10–40 μm range. At intermediate dwelling time (1.5 h, Fig. 6B), large clusters, when present, are in the 70–200 μm range, make most of the volume, and also yield 10–40 μm bubbles. At the scale of these sub-volumes, the respective distributions of original and de-coalesced samples can be nearly identical, regardless of whether they are permeable or not (compare B2 and B4 in Fig. 6B). As clusters are mostly formed during the time lapse covered by series A and B, the narrow range of the de-

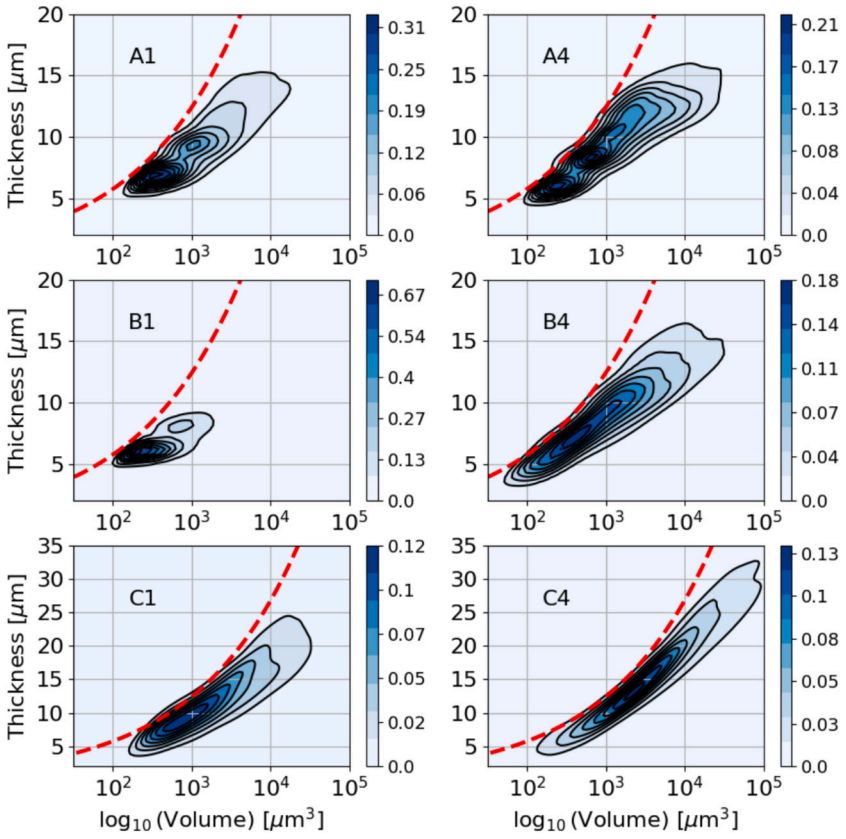

Fig. 4. Bubble thickness as a function of bubble volume for the same representative samples as in Fig. 3. The colour gradients indicate normalized densities that were calculated by Gaussian kernel density estimation. Dashed red lines indicate the thickness (diameter) behavior of spheres.

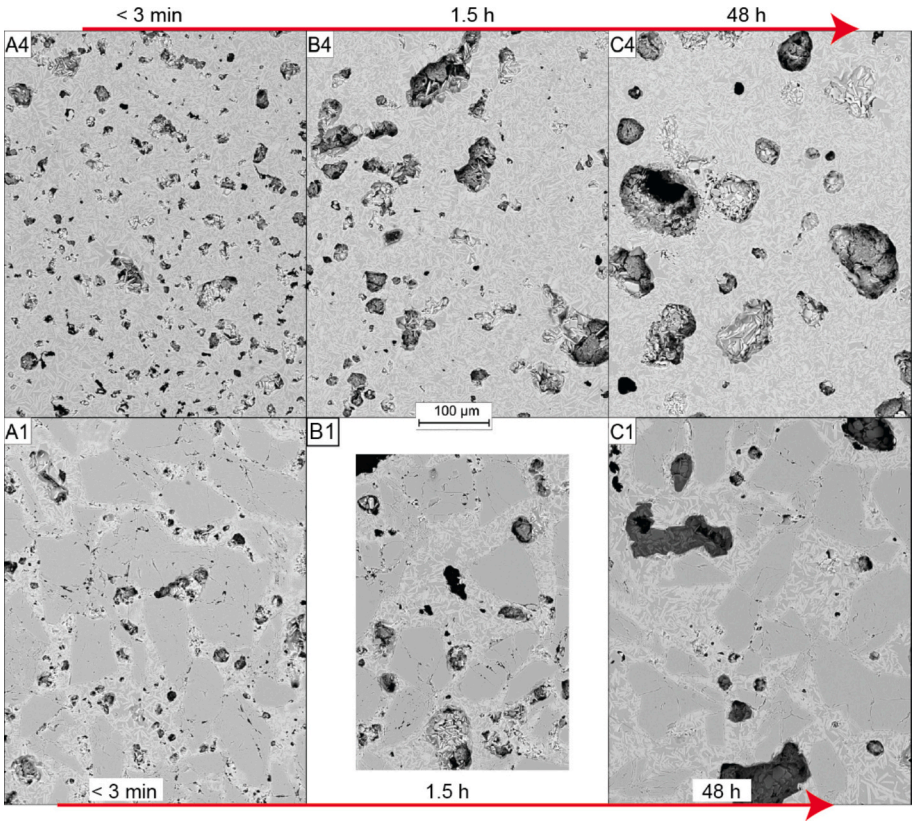

Fig. 5. SEM images of the two times series A4-B4-C4 and A1-B1-C1 illustrating the effect of dwell time on bubble sizes. All images are at the same scale. Associated bubble size distributions are shown in Fig. 3. The bubbles in Image C1 have been darkened to facilitate bubble visualization (original SEM image is in Supplementary material Fig. S6).

coalesced population suggests that clusters form, at least partly, by successive addition of bubbles with equivalent diameters of 10–40 µm. At long dwelling time (48 h, Fig. 6C), a few 70–100 µm clusters are present and they are made of 20–40 µm parent bubbles (sample C6). These clusters have thus a similar composition as those at intermediate dwelling time. The largest clusters are >100 µm and they cannot be separated as they have nearly spherical shapes (Fig. 4), thus yielding de-coalesced clusters 30–100 µm (sample C1).

Fig. 7 shows a measure of cluster shape done on the same µCT sub-volumes as those used for bubble de-coalescence. This measure is the ratio between the longest axis of an ellipsoid fitting the cluster dimensions and its equivalent diameter (i.e. the diameter of a sphere of identical volume). Large ratios correspond to clusters that form extensive, unidirectional bubble chains, whereas ratios closer to one indicate more isotropic clusters and/or clusters containing few bubbles. Without de-coalescence, samples from series A and C have ratios <20, whereas those of series B reach ratios of 70. Fig. 7 suggests that bubble clusters form progressively longer chains as dwelling time approaches 1.5 h and then they become more isotropic as dwelling time reaches 48 h. It suggests that some impermeable samples (such as B8) contain long chains that might lead to percolation under slightly different conditions.

Fig. 8 shows, for the same seven samples, the density distribution of the major and minor axes of the de-coalesced bubbles. The populations of bubbles with equivalent diameters of 10–40 µm present in series A and B are not spherical; they have complex shapes that are <15 µm in their smallest dimension and that reach up to 30 µm in their longest dimensions. Most have shapes with an aspect ratio of ~2, a longest axis of ~10 µm, and a shortest axis of ~5 µm, which suggest that they have themselves undergone various degrees of coalescence. This is consistent with the average thickness of at most 15 mm measured on the full (without de-coalescence) clusters (Fig. 4). The de-coalesced bubbles of series C, however, are closer to spheres, which is also consistent with the data on the full clusters of Fig. 4.

Determining the total bubble number densities of our samples is difficult because the shapes of bubble cluster differ significantly from spheres (Fig. 7), and because total number densities are dominated by small bubbles (Fig. 3B and D) that are best captured by 2D SEM images. The 2D distributions of representative samples were converted into 3D using stereological methods that either ignore or depend on object shape before being summed to obtain total number densities. Fig. 9 compares the number densities obtained by these two stereological methods with those obtained using the µCT volumes alone. The number densities from µCT volumes are 1 to 2 orders of magnitude lower than those from SEM images. The discrepancy seems to be lower for samples without phenocrysts (i.e. sample labels ending in 4 and 8). Numbers from the two stereological methods are similar, probably because the smallest bubbles are correctly approximated by spheres. Both methods, however, are likely to overestimate the number of small bubbles when chains are present (i.e. cluster sections appear as series of small circles that are not corrected for by either method). Overall, Fig. 9 suggests that the number densities are not correlated with dwelling time. This observation, the combined uncertainties of the measurement methods, and the nature of the smallest, most numerous bubbles (whether nucleated during the experiment or Ar gas residues) led us to consider bubble number densities as poor indicators of coalescence and nucleation. For consistency with the other measured parameters, we simply reported in Table 2 the number densities with respect to the melt obtained from the µCT volumes. These number densities are not correlated to any other parameters (Supplementary Material Fig. S7).

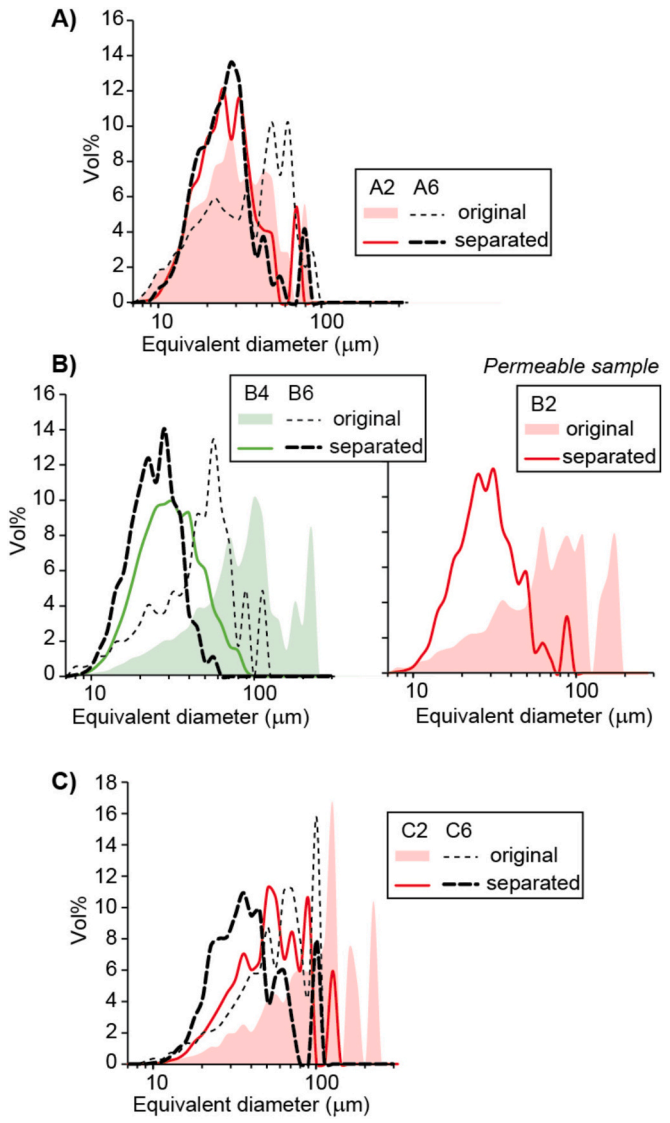

Fig. 6. Bubble size distribution of sub-volumes with interconnected bubbles (original) and bubbles de-coalesced in a semi-automatic fashion (separated). The Y-axis labeled "Vol%" corresponds to the proportion of gas volume distributed within every bubble size bin. All samples are impermeable except B2. A) Series A. B) Series B. C) Series C. Additional data on bubble size distributions can be found in Supplementary material 2.

3.2. Coalescence

The process of coalescence, defined as the agglomeration of several bubbles to form a cluster, can be observed in our samples at various stages of completion. Visual inspection of the SEM images shows that mostly bubbles from class β take part in the early coalescence process. This pre-coalescence stage corresponds to the juxtaposition of several bubbles separated by thin melt films (Fig. 10A). The rupture of this film (Castro et al., 2012a) creates a coalesced final bubble. Its post-coalescence shape is elongated, similar to that of the original juxtaposed bubbles. Post-coalescence, chain of bubbles still shows the remnants of the bubbles that were used to form it (Fig. 10B). Such a feature, as illustrated in Fig. 10A, is scarce in our samples. This paucity is partly due to the SEM method, which implies having the sample cut in the proper 2D plane to capture the geometry of the coalescing bubbles (which cannot be constrained beforehand) and also due to the short timescale of film rupture (discussed in Section 4.1.1). As shown in the multimodal distributions of Fig. 6, the coalescence of γ-class bubbles occurs in two broad stages, many <50 μm bubbles giving rise to a cluster >50 μm. We also observe that large bubbles (γ or δ) can also agglomerate β-class bubbles when in proximity, although the data of Fig. 6 suggest that it is not the dominant cluster growth mechanism.

We define herein that the bubble curvature radius is the radius that fits the local curvature of a bubble. In this study, curvature radii can easily be deduced since many post-coalescence bubble clusters have shapes still bearing the shape of the parent bubbles (Fig. 2B, Fig. 10B). Smaller radii of curvature generate larger surface tension forces on these partly retracted bubble walls (Bagdassarov et al., 2000).

For isolated and smooth bubbles, the radius of curvature is very close to the equivalent radius of the bubble itself (i.e., they are close to spherical, Fig. 2C). Bubbles with protruding microlites have local radii that are much larger than the equivalent radius, as can be observed in Figs. 2B and 10B. Between each microlite, the curvature of the bubble interface with the melt has a diameter equal to the spacing between the two adjacent microlites. This arrangement implies very high local surface tension forces compared to isolated or smooth bubbles.

3.3. Permeability

Gas permeability measures the ability of the gas to percolate in the matrix made of melt and crystals (Supplementary material Table S3). In series A, only one sample (A3) is permeable, with 9.6 vol% bulk gas and 72.7 vol% total of crystals. In the B series, four samples (B1, B2, B3, and B5) are permeable, all with gas quantities below 10 vol% bulk and over 65 vol% crystals. In the C series, the only permeable sample (C5) has 9.2 vol% bulk of gas and 70.7 vol% crystals. Our data show that no sample with less than 7 vol% bulk of gas is permeable (Table 2). All the samples without alumina crystals (see samples A4, B4, and C4 in Figs. 3 and 5) are impermeable. Fig. 1 shows that samples composed of only melt and microlite have the highest gas content (~15 vol% bulk compared to ~8 vol% bulk in samples with alumina crystals) due to their smaller total crystal content. This larger bulk gas content of samples without alumina is however not correlated with the presence of percolating bubble chains (Supplementary Material Fig. S7A: alumina-free samples have higher gas content but are not permeable, unlike alumina-rich samples, which have a significantly lower gas content yet permeable channels) and remains an insufficient condition for percolation to occur.

Percolating samples are permeable in 1 direction (B2, B3, B5, and C5), 2 directions (B1), or 3 directions (A3) (see the number of stars symbols in the K_g column of Table 2). When percolating in several directions, the permeability values are comparable regardless of the direction (supplementary material Table S4), which suggests an isotropic percolating network. In other words, there is no significant variation in permeability values between 1D-permeable and 2D-permeable samples. Sample A3, which is permeable in 3 directions, has the highest permeability despite being in the same range of gas content as the other permeable samples. The capsules orientation in the IHPV is known, and there is no significant correlation between the directions of permeability of the percolating chains and that of gravity. The K_g values of our samples range from 1.0×10^{-14} to 1.9×10^{-13} m^2 without any significant dependence on crystal size (Table 2 and supplementary material Table S4). The range of gas content of our permeable samples is narrow, which explains why we do not observe significant permeability variation between them. Even if each series has at least 1 permeable sample, the majority of permeable samples occur in series B, which has a dwelling time of 1.5 h. This finding implies that the dynamics of percolating chains depend on dwelling time. The other control of this dynamics is the gas content (Theurel et al., 2024). Fig. 1 suggests that the variability in initial conditions caused some A- and B-series samples to have gas content too low to yield percolation.

Since no differential stress was applied to the samples during the experiments, there is no reason to suspect a pressure gradient across the samples; the deformed aspect of some bubbles may, therefore, not be attributed to external deformation. Our analyses and visual inspection of

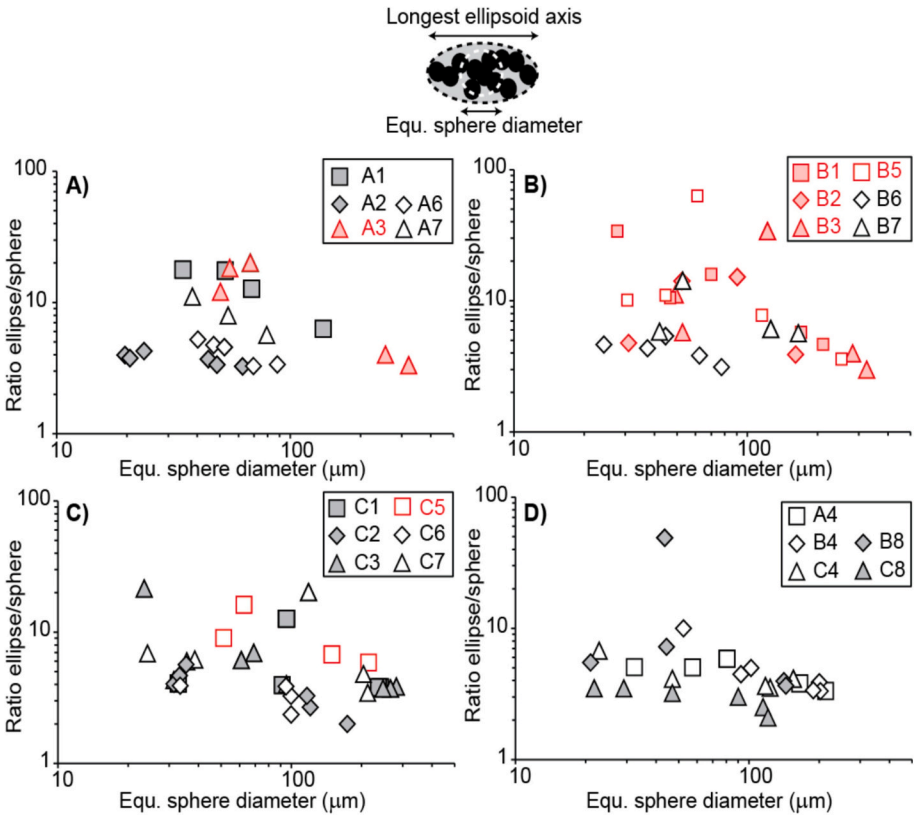

Fig. 7. Bubble cluster shapes as a function of cluster size (see 2D illustration atop). Symbol colour indicates whether samples are permeable (red) or not (black). A) Phenocryst-bearing series A samples. B) Phenocryst-bearing series B samples. C) Phenocryst-bearing series C samples. D) Samples without alumina phenocrysts.

the samples allow us to conclude that the formation of permeable chains is due to the process of bubbles coalescing from one individual to the next. The potential elements at play are capillary, viscous, and gravity forces, as well as diffusion of dissolved water. We call this permeability primary because it arises from the first bubbles present in the magma, which have undergone rapid growth through decompression, and because it occurs prior to any external deformation.

4. Discussion

4.1. Time scales from coalescence to percolation to relaxation

Our observations show that coalescence depends on time (Fig. 5). For samples with short dwell times, coalescence is incipient. The bubble class β is mainly observed in these samples. In some places, coalescence is about to take place (in SEM, we can still see melt films preventing bubbles from coalescing, Fig. 10A) or has just happened (Fig. 6A and remnant shape of the bubbles that formed the chain, Fig. 10B). After 1.5 h under dwell conditions (series B), the chains are well established (Fig. 6B), which is why we counted the largest number of permeable samples in this series. Finally, if the system is maintained closed for long enough without external deformation, the chains partition into larger spherical bubbles, as we observe in series C (Figs. 6C and 5).

4.1.1. Processes driving bubble coalescence

The formation of permeable chains by bubble coalescence in crystal-bearing magmas is a well-documented phenomenon supported by numerous experimental and numerical studies. In experimental research, primary permeability has been shown to arise above a rather broad range of bulk gas content, 35–80 vol%. For instance, deGraffenried et al. (2019) present permeable samples above 55% porosity, a finding corroborated by Lindoo et al. (2017). Lindoo et al. (2016), on the other hand, demonstrate the existence of permeable samples between 70 and 80% porosity. More recently, Graham et al. (2023) presented permeable samples with 35% porosity. In natural samples, there is no guarantee that primary permeability is preserved. Permeable pumices are found to have a possible 30% porosity threshold (Mueller et al., 2005). A fairly comprehensive summary of permeable natural samples can be found in Wright et al. (2009). Conversely, low-porosity natural samples have been found to be permeable due to microcracks, as demonstrated by Mueller et al., 2005, or in lower-viscosity magmas, as in Saar and Manga (1999). Numerically, Parmigiani et al. (2017) propose a permeability relationship between crystal content and critical porosity under conditions such that bubbles move by buoyancy. To reproduce conditions prevailing in a deep volcanic conduit (≈5 km) during inter-eruptive time, our study produced samples with bulk porosities (7–15 vol%) lower than those previously explored, by previous studies, in vesiculation and channelling experiments (such as in Graham et al., 2023, with 35 vol%, or in deGraffenried et al., 2019, with 55 vol %) as well as in a deformation-free environment that precludes fracturing.

We assessed four physical processes that could control the initiation of coalescence. The first process, buoyancy, was already deemed unlikely to play a role by Theurel et al. (2024) because the Bond numbers of our experimental conditions (10^{-6}–10^{-4}) indicate that surface tension forces largely dominate gravity forces. Coalescence can occur when bubbles grow in close proximity (Castro et al., 2012b). If the decompression took place fast enough, bubbles could still be growing at the beginning of the dwell time. We thus quantified whether bubbles grew in equilibrium during decompression. The growth time (τ_g) of bubbles by gas expansion is estimated by Okumura et al. (2019) as:

$$\tau_g = \frac{\eta}{\Delta P} \quad (1)$$

where η is the strain-rate-dependent magma viscosity (Caricchi et al., 2007) and ΔP is the pressure difference between the bubble and the

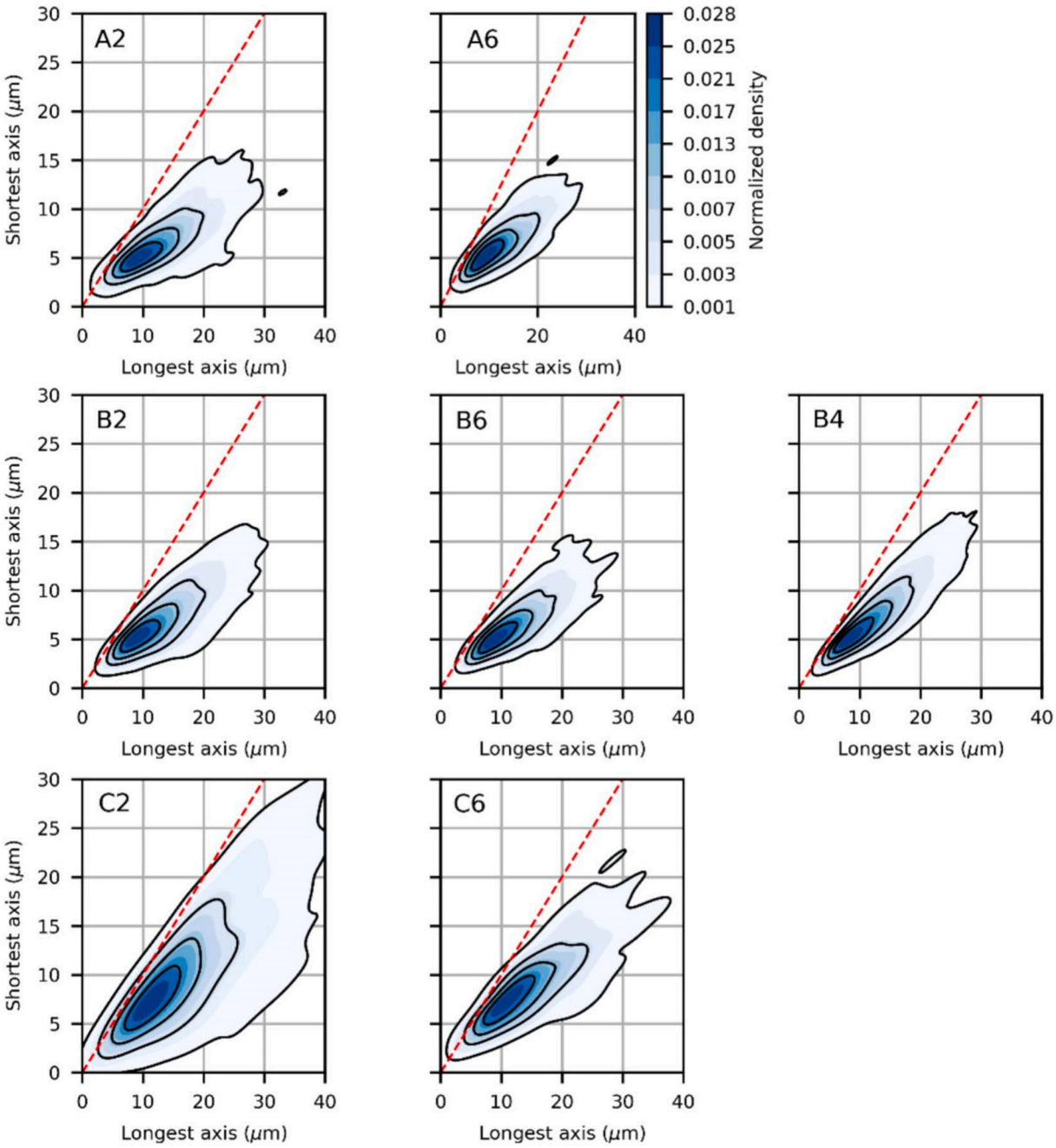

Fig. 8. Density distributions of the shortest and longest axes of the ellipsoids fitted to the de-coalesced bubbles from the same samples as in Figs. 6 and 7. The normalized densities were calculated by Gaussian kernel density estimation.

surrounding medium. The viscosity of the melt-crystal mixture of each sample is calculated as:

$$\eta = \mu\eta_{rel} \quad \text{with} \quad \eta_{rel} = \left(1+\left(\frac{\varphi_C}{\varphi_{Cm}}\right)^{\delta_1}\right)\left(1-\alpha_1 erf\left\{\frac{\sqrt{\pi}}{2\alpha_1}\frac{\varphi_C}{\varphi_{Cm}}\left[1+\left(\frac{\varphi_C}{\varphi_{Cm}}\right)^{\gamma_1}\right]\right\}\right)^{-B_1\varphi_{Cm}} \quad (2)$$

where B_1, α_1, β_1, and γ_1 are strain-rate-dependent fitting parameters and φ_{Cm} is the maximum solid packing fraction, all described in Caricchi et al. (2007). The variable μ is the melt viscosity ($10^{4.6}$ Pa s) and φ_C is the crystal content. The viscosity of the melt-microlite mixture is $\sim 10^5$ Pa s for alumina-free samples and the viscosity of the whole mixture of melt-phenocryst-microlite is $\sim 10^{10}$ Pa s. When using strain-rate-dependent magma viscosity, we consider bubble growth to be the only phenomenon causing strain in our samples. As the bubble grows during the 350 to 120 MPa decompression strain is localized at the melt-gas interface. As the growth time of the bubble depends on the viscous resistance of the complex surrounding medium, we calculate the time scale for two situations. If the bubble grows close to an alumina phenocryst, growth implies the displacement of both microlites and phenocrysts suspended in the melt. In this situation (Fig. 11), $\tau_{g(Al+Pl)}$ considers the viscosity of the bulk suspension. If the bubble nucleates and grows far from phenocrysts, only the microlites and melt resist bubble growth. Thus, $\tau_{g(Pl)}$ considers the viscosity of the melt plus microlites. For each case, we also bracketed the values of relative viscosity depending on strain by considering a minimum, negligible expansion, and a maximum expansion, where the deformation rate is approximated by the maximum gas volume expansion, ~10 vol% (the median bulk gas content of all our samples is 9.47 vol%, Table 1), divided by decompression time.

In this study, we only consider $\tau_{g(Pl)}$ as the initial bubbles are smaller

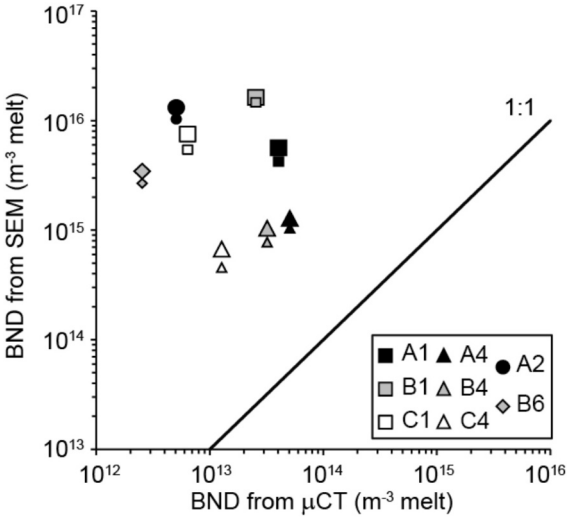

Fig. 9. Bubble number densities (BND) from SEM images using the Cheng and Lemlich (1983) 2D-3D correction (small symbols), and SEM images using the Sahagian and Proussevitch (1998) 2D-3D correction (large symbols) as a function of the that calculated from the µCT volumes. Data are listed in Supplementary Material Table S2.

than the characteristic microlite size. The calculated $\tau_{g(Pl)}$ is systematically shorter than the three dwelling times of our series (the three pink dashed curves; Fig. 11). The maximum bubble overpressure caused by the decompression of the samples when ignoring growth (gray dotted line in Fig. 11) intersects $\tau_{g(Pl)}$ around 1 MPa, which means that bubbles have a maximum overpressure of 1 MPa. This overpressure neglects that growth is a dynamic process, which implies that the calculated $\tau_{g(Pl)}$ is on the high end of the real values. This means that no matter the amount of overpressure in the bubble during and after decompression, the timescale of bubble growth due to this overpressure is systematically smaller than the decompression duration and the smallest dwelling time (<500 s). Bubble also grow by addition of dissolved water diffusing from the melt to the bubble wall. Using a diffusion coefficient of 1.3×10^{-10} m^2/s (Nowak and Behrens, 1997), the characteristic diffusion distance is 154 µm during the 3 min. of decompression time, which is large enough to ensure that bubble growth was not limited by sluggish diffusion. In other words, bubbles can be considered to have reached and maintained equilibrium sizes before decompression ends for our three series.

As growth-related coalescence is unlikely, we quantify whether bubbles could move under capillary forces once their equilibrium sizes is reached. Depending on the bubble position relative to the surrounding plagioclase microlites, several scenarios can unfold during the tail end of decompression and the early stages of the dwelling time. If a bubble is originally located next to two (or more) plagioclases when decompression causes bubble growth, it can be constrained by both microlites, yielding a deformed bubble confined in the wedge formed by the two microlites. The dynamics of such a situation have been studied by Reyssat (2014), who concluded that this constriction leads to variabilities of capillary forces along the bubble surface. The combined effect of these forces drives the displacement of the bubble in the opposite direction to the tip of the wedge formed by the microlites. As this displacement is driven by the microlite sides, we consider that the maximum displacement caused by this phenomenon is on the order of the microlite length (around 10 µm).

The displacement of the bubble as a function of time follows two regimes depending on the distance from the wedge tip (Reyssat, 2014):

$$x_1(t) = \frac{\alpha\sigma}{6\mu}t \tag{3}$$

$$x_2(t) = \left[\frac{13\sigma}{8\sqrt{2}\,\mu\chi^{3/2}}\left(\frac{\Omega}{\alpha\pi}\right)^{3/4}(t-t_0)\right]^{4/13} \tag{4}$$

where x_1 (x_2) is the distance covered by capillary displacement in the first (second) regime, α is the wedge aperture angle made by the two microlites, σ is the gas-melt surface tension (0.07, Gardner et al., 2013), µ is the melt viscosity, χ is a constant (=1.32, Reyssat, 2014), Ω is the volume of a bubble. The two regimes differ in the dominant mechanism of viscous dissipation (Reyssat, 2014). The transition occurs when the primary source of dissipation shifts from bulk viscous effects (when the bubble is tight in between the microlites and under very high stresses) to contact-line dissipation (when there is a weaker confinement of the bubble and friction with the microlites becomes non-negligible, i.e. localized dissipation). Close to the wedge tip, at $x(t=0) = x_1 = 0$, where x is the global displacement, the bubble travels at a constant speed given by Eq. (3) that is proportional to α. Further away from the tip, the bubble decelerates according to Eq. (4), which is inversely proportional to $\alpha^{3/13}$.

The transition between the two regimes occurs when the critical time, t_b, is reached:

$$t_b = b\frac{\mu}{\sigma}\Omega^{\frac{1}{3}}\alpha^{-\frac{16}{9}} \text{ with } a = 3^{\frac{2}{3}}6^{-\frac{2}{9}}\pi^{-\frac{1}{3}} \text{ and } b = 6a\chi^{-\frac{2}{3}} \tag{5}$$

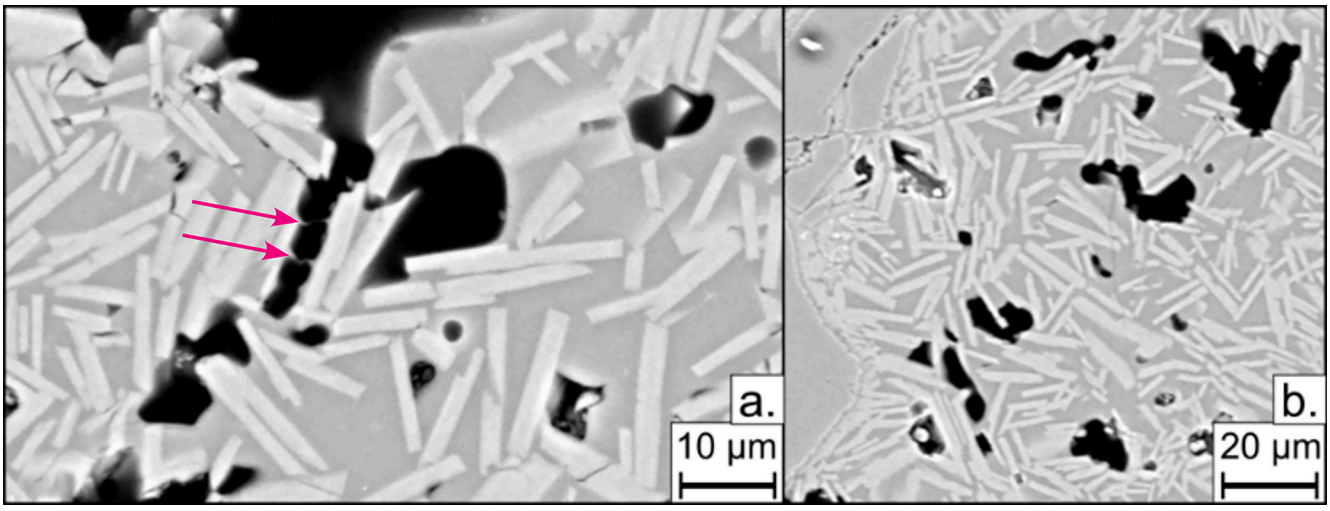

Fig. 10. SEM images of sample A7 showing a.) A pre-coalescence bubble chain (pink arrows highlight the film of melt between the isolated bubbles), and b.) A post-coalescence bubble chain (or cluster).

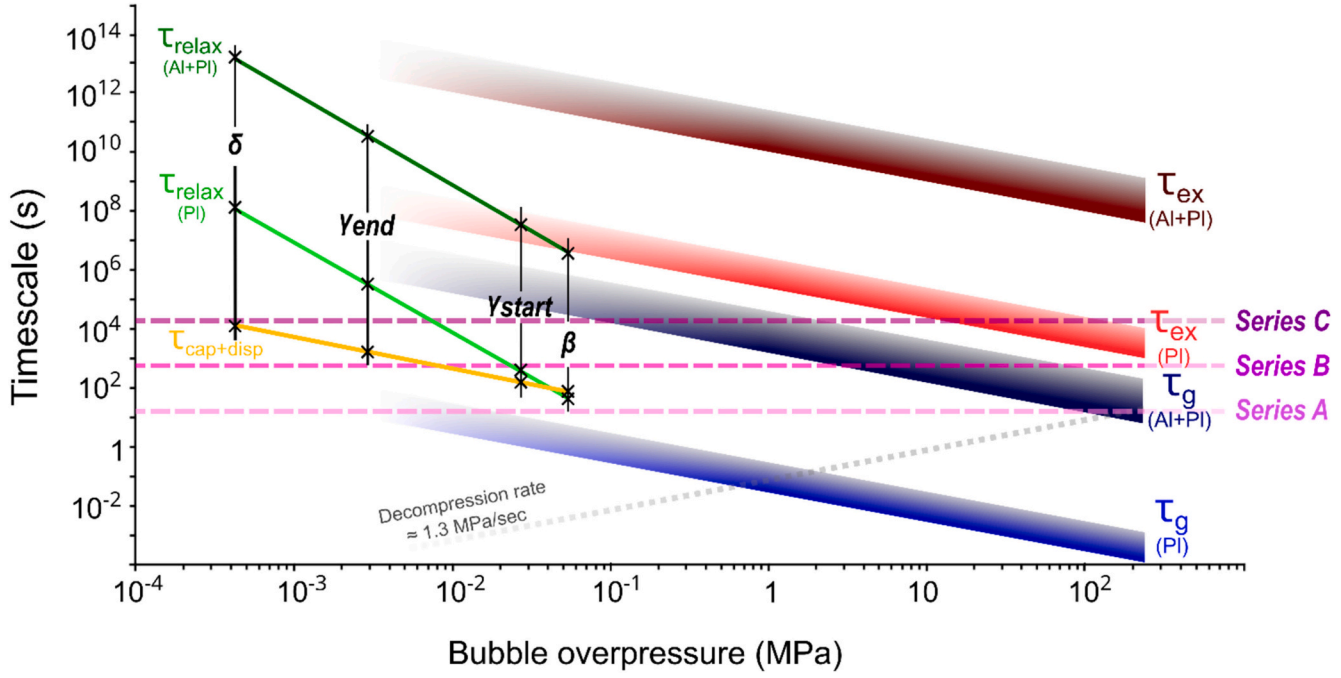

Fig. 11. Estimated timescales of gas bubble growth (blue), gas extraction (red), bubble relaxation (green), and melt film thinning by capillary forces (yellow). Ranges for τ_g and τ_{ex} are calculated with different relative viscosities depending on strain. τ_{relax} and $\tau_{cap+disp}$ (sum of τ_{cap} and τ_{disp}) are calculated with the mean significant bubble radius of each bubble class presented in Fig. 3.For τ_g and τ_{ex}, we decided to lighten the part with the lowest bubble overpressure to allow good visibility of $\tau_{cap+disp}$ and τ_{relax}. The dotted line marks the applied decompression rate before dwelling. Pink dashed lines correspond to dwell times of series A, B, and C from bottom to top. Black lines correspond to the maximal bubble overpressure according to the radii of curvature of each characteristic bubble size class. As the γ class spans a large range of bubble size, we added the labels γ_{start} and γ_{end} to highlight the smallest and largest bubbles included in the γ class, respectively.

The time delay t_0 in Eq. (3) corresponds to the time at which $x_1 = x_2$ when $t = t_b$, which yields:

$$t_0 = t_b - a^{\frac{13}{4}} \frac{8\sqrt{2}\mu}{13\sigma} \pi^{\frac{3}{4}} \Omega^{\frac{1}{3}} \chi^{-\frac{1}{3}} \alpha^{-\frac{16}{9}} \quad (6)$$

The bubble grew enclosed by microlites, which is a prerequisite to apply Reyssat's capillary displacement. We neglect bubble growth during capillary displacement as it will increase the speed of the bubble in the wedge and enhance this phenomenon. During this displacement, the bubble will only be facing the melt, and consequently, in this equation, we use the melt viscosity, μ, instead of the strain-dependent viscosity used in Eq. (2).

The results of the model of Reyssat (2014) are shown in Fig. 12. We

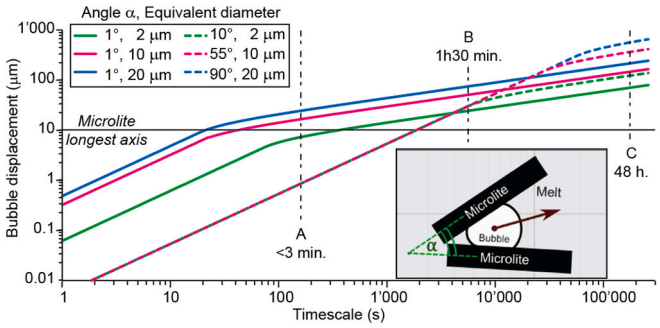

Fig. 12. Estimation of bubble cumulative displacement triggered by bubble growth in the wedge formed by two adjacent microlites according to Reyssat, 2014. Calculations were made for bubbles with 2, 10, and 20 µm equivalent diameter (solid lines from bottom to top, respectively). Solid lines correspond to the displacement with the maximum angles for the given bubble size. Conversely, the dotted lines correspond to a minimum angle of 1°. The dark gray dashed line marks the typical microlite size. Inset: Schematic of the capillary displacement described by Reyssat (2014).

first assume that the bubble grew close to the edge so that $x(t = 0) = x_1 = 0$. The displacement of a bubble through time is calculated for three typical bubble sizes: 2 µm equivalent diameter representative of the smallest bubbles, 10 µm for the low end of the γ-class, and 20 µm for the median size of the bubbles de-coalesced from the clusters (Fig. 6) with associated maximal angle (Fig. 12, solid lines). For the two smallest sizes, the maximum wedge angle at which the bubble is constrained (and thus loses its spherical shape) considering the whole microlite length of 10 µm is calculated using trigonometric relationships that yield respective angles of 11° and 60°. We assumed a maximum angle of 90° for the 20-µm case as the geometry with such large bubbles implies that the two microlites do not touch each other as depicted in Fig. 12 but are located at some distance from each other. We also performed the calculation for the same respective bubble sizes but with a minimal angle of 1° (dotted lines). As expected, the initial speed decreases when the wedge angle decreases as the bubble pulls away from the wedge tip because Eq. (3) controls the beginning of the displacement.

In the case of wide angles (Fig. 12, solid lines), every bubble has traveled within 180 s for at least two times its size. As our decompression lasts ~180 s and the minimal dwelling time is 60 s (series A), some of our experimental bubbles have thus likely been subjected to capillary motion as soon as dwelling starts. If we consider that 10 µm is the typical microlite length (the full range is 4–15 µm, Theurel et al., 2024), we can deduce that the capillary motion of bubbles larger than 20 µm equivalent diameter cannot be described by Eqs. (3)–(4) unless microlites are aligned because their geometry is no longer that of a bubble squeezed between two plates. This threshold of 20 µm is also the apparent limit between isolating and perforating microlite behavior (Fig. 2D). Both of these statements, in turn, are consistent with the fact that bubbles smaller than 20 µm equivalent diameter are either constrained or displaced in presence of microlites. In addition, as the typical microlite length scale is taken to be the maximum bubble displacement length, we deduce that, by the timescale of series B (1.5 h), every constrained bubble has been displaced by at least 10 µm at the maximum wedge

angle.

For narrower wedges, the first regime (which applies close to the wedge tip) is dominant over longer timescales and yields a smaller displacement compared to larger angles. Once the transition to the second regime happens, speeds are higher than for larger bubbles. In the timescales explored in this study and for small angles, the transition between the two regimes occurs later than the timescale required to reach the microlite length scale.

If we assume that the bubble grew further from the edge such that $x(t = 0) = x_2 = 0$ with $t_0 = 0$, the capillary speed is solely controlled by Eq. (3). The breaks in slope in Fig. 12 suggest that this situation happens when bubbles are at least 5–6 μm away from the edge when angles are large. Eq. (5) indicates that it takes only 20–90 s to reach this transition, inducing a minimal acceleration over the timescales of interest compared to the $x(t = 0) = x_1 = 0$ case. When $\alpha = 1°$, the acceleration is larger, but the transition happens 30–150 μm away from the edge, which is longer than the microlite longest axis. So, our first assumption that the bubble grew close to the edge yields minimal estimates of the capillary speed, which is appropriate to assess whether this process occurred in our experiments.

It is thus likely that bubbles came in close proximity due to the interplay between capillary forces and bubble–microlite interactions. These bubbles are then separated by a melt film that can deform and rupture under further action from capillary forces. The coalescence of two bubbles separated by a melt film has been quantified over time by Castro et al. (2012a) and Giachetti et al. (2019). This film-thinning time is estimated as:

$$\tau_{cap} = \xi ln\left(\frac{\delta_0}{\delta_f}\right)\frac{\mu R}{\sigma} \quad (7)$$

Where ξ is an empirical constant (=20, Nguyen et al. (2013)), δ_f is the final thickness of the melt film before rupture (estimated to be 100 nm, Giachetti et al. (2019)), R is the average bubble radius, and δ_0 is the initial film thickness. δ_0 is estimated to be between 2 and 3 μm (e.g., Fig. 10), although setting it to 0.5 or 10 μm would only change the timescale by a factor 0.5 and 1.5, respectively. To place τ_{cap} for our different bubble size classes into the time-overpressure diagram of Fig. 11, we calculated the maximum overpressure of bubbles having the characteristic radii of curvature of each class. It is estimated by:

$$\Delta P_{class} = \frac{2\sigma}{R} \quad (8)$$

These values must be considered only as indicators of the expected range of value of τ_{cap} and τ_{relax} (see below) as a function of the initial size of the bubble coalescing (or relaxing, see below). Unlike τ_g, we consider that only melt is displaced by the capillary forces. Thus, τ_{cap} is independent of the bubble proximity to any crystal. Using the equivalent bubble radii of the different size classes defined in our experiments, the time taken to observe film thinning by drainage until rupture lies around 4 min for the smallest bubbles (Fig. 11). Nevertheless, as we observe that mostly β class and early γ class bubbles are involved in the coalescence process (Figs. 3 and 6), we can reduce the capillary film-thinning time to 15 to 30 min by only considering these two classes (Fig. 11, intersections between yellow line τ_{cap} and the bubble overpressures corresponding to β and γ_{Start}). This quantification is corroborated by our experimental results from series A, showing melt films still separating bubbles (Fig. 10A). This immature coalescence quantified by τ_{cap} is consistent with the paucity of permeable chains in the A series. If the shapes of the δ-class were closer to a sphere, the coalescence of the bubbles would take more than 30 h. However, given their very elongated and tortuous shape, and thus the small size of the local curvatures, this value should be considered a maximum.

Here, τ_{cap} represents the time required for two bubbles to coalesce once they are close enough (spacing of δ_0). We describe in Fig. 12 that most bubbles have already reached a distance equivalent to a microlite length before the first dwell time due to capillary displacement. As this displacement is the first parameter fostering coalescence (i.e. capillary film-thinning and rupture), we have to consider both the time for capillary displacement, τ_{disp}, and τ_{cap} to evaluate the real coalescence timescale. Fig. 12 suggests that $\tau_{disp} = 180$ s is a minimum timescale to generate a bubble displacement large enough to foster bubble proximity and capillary film rupture. Consequently, the minimum complete timescale required for coalescence is around $\tau_{disp} + \tau_{cap}$. This timescale is variable within one sample, as it depends on bubble size (which is characterized by a wide range of values). That timescale is generally close to the timescale for decompressing and quenching of series A. Film rupture and partial retraction are almost instantaneous processes once the critical spacing between the bubble is reached, which explains why we only rarely observe cases of near-coalescence on SEM images (Fig. 10A).

4.1.2. Formation of permeable bubble chains

Following the rupture of the melt film, the resulting bubble has a shape with the length of its long axis close to the sum of the diameters of the two bubbles involved in the coalescence (Fig. 10). Just after coalescence, tension forces are strongest and mostly heterogeneous at the bubble surface. The bubble shape is elongated, and tension forces are concentrated at the smallest radii of curvature, with the aim of restoring a spherical shape. Larger bubbles take longer to relax due to the quantity of microlites and melt to be displaced to achieve a spherical shape (Larsen and Gardner, 2000; Okumura et al., 2012). The relaxation time is estimated by using a modified version of the gas extraction timescale defined by Okumura et al. (2019), which characterize the timescale required for the migration of an effective fluid through a permeable medium under the effect of a pressure gradient, $\Delta P/l$::

$$\tau_{relax} = \frac{l^2 \varphi_{tot} \eta_{min}}{K_{i,tot} \Delta P} \quad (9)$$

where η_{min} is the strain-rate-dependent magma viscosity for zero strain rate (Eq. (2)). The characteristic length, l, is given by the bubble diameter, $2R$, and the pressure difference, ΔP, is given by Eq. (8). Note that Eqs. (8)–(9) can be recast into the relaxation time of a bubble suspended in a pure fluid (e.g., Larsen and Gardner, 2000) times a correction factor for the effect of the permeable flow of a mixture:

$$\tau_{relax} = \left(\frac{\mu R}{\sigma}\right)\left(\frac{R^2 \varphi_{tot} \eta_{rel}}{8 K_{i,tot}}\right)$$

In this calculation, we consider the local strain as vanishing because relaxation occurs after growth. The variable $K_{i,tot}$ is the intrinsic permeability that quantifies the resistance offered by the interstitial space between microlites and phenocrysts to the motions due to the bubble regaining sphericity (Supplementary Material Table S5, Text S1). The comparison between τ_{relax} and the other timescales calculated in this study is presented in Fig. 11. Here, we also considered two scenarios, depending on the crystalline charge, which are representative of our two types of crystalline composition: microlite only (~45%) and microlite-phenocryst (~70%). The bubble relaxation timescale if the bubble is only surrounded by the melt-microlite mixture, $\tau_{relax(Pl)}$, is faster to relax small (β) bubbles than to coalesce them ($\tau_{cap} + \tau_{disp}$). For larger bubbles (γ and δ), $\tau_{relax(Pl)}$ is systematically larger than the capillary displacement and capillary coalescence timescale. On the other hand, the relaxation timescale in an alumina-melt-microlite mixture, $\tau_{relax(Al+Pl)}$, is systematically higher than the required coalescence timescale (up to nine orders of magnitude higher). So, τ_{relax} is generally longer than the time required for two or more bubble chains to coalesce.

As a result, increasingly long chains of bubbles coalesce until they form channels (Figs. 6 and 7) that percolate through the entire sample, which is fostered by the geometry of the microlite interstitial space (Oppenheimer et al., 2015). In alumina-free samples, we can still observe signs of coalescence but a poor wider connectivity (Fig. 7D). This might reflect that bubbles are closer together when alumina is

present because bubble number densities with respect to the melt are slightly higher in that case (Table 2).

4.1.3. Evolution of the permeable chains

Once the permeable chains are formed, the gas can theoretically flow freely inside the percolating pathways through the sample (Theurel et al., 2024; Yokoyama and Takeuchi, 2009). If gas circulated freely through the gaseous networks, as it would in a volcano, we can hypothesize that the gas pressure on the inner walls of the channels would allow these channels to remain open for as long as gas inlet is supplied. This would, in turn, allow the gas stored deeper to percolate to shallower levels (Caricchi et al., 2024; Christopher et al., 2015; Collombet et al., 2021) or escape from the conduit over longer timescales. In other words, outgassing is fundamentally an open-system process in natural systems.

Unlike a volcano, our system is strictly closed. No pressure gradient is applied in our capsules to cause gas to move through the channels, and no gas flow is imposed at the percolating chain inlet or outlet so that bubble chain relaxation to sphericity can be observed (Fig. 5). The phenomenon of regaining sphericity displaces the surrounding melt and microlites, which, in turn, disturbs the surrounding chains. For long dwell times, such as 48 h, bubbles are visually more spherical (Fig. 5, samples C1 and C4), which is corroborated by the theoretical estimation of their relaxation timescale (Fig. 11, $\tau_{relax(Pl)}$). After 48 h, relaxation has occurred for almost all bubble sizes, even for most permeable chains (δ-class in series B). Thus, only a few δ-class bubbles are theoretically still as chains and clusters after this dwell time (Fig. 11), which explains why permeable chains are still present in one sample (C5). Chains, however, span large distances (Fig. 7), even percolating across the sample (as seen on δ-class illustrating panel of Fig. 3), and relax over similar time scales (Fig. 11). A simultaneous and complete reorganization of intertwined chains into a series of corresponding spheres is thus unlikely. We speculate that the complex melt–crystal medium deformation caused by relaxation fosters chain breakup (hypothesis described in the next paragraph). In alumina-bearing samples, we expect that the rigid alumina framework exacerbates breakup (Supplementary Material Fig. S8, Video S2). Nonetheless, the theoretical relaxation timescales are calculated for a constant bubble size. The relaxation timescale we calculated for the largest permeable chain is valid only as long as the chain remains unbroken. If the chain ruptures, we have to revaluate the relaxation timescale for the new smallest bubble size, implying a faster relaxation.

Several reasons lead us to propose that the partition of permeable chains leads to multiple spherical bubbles instead of one. Firstly, in our samples and samples from the literature (Rust and Cashman, 2004; Wright et al., 2009, 2006a, 2006b), bubbles are initially numerous, small, and homogeneously distributed (as in Fig. 5, sample A4), whereas typical permeable chains in our samples range between 400 and 800 μm in equivalent diameter (δ class). The partition of such chains would lead to several γ-class bubbles: a few bubbles if it partitions into 100 μm γ-bubbles to hundreds of bubbles if the daughter bubbles are smaller. Fig. 3A and C suggest that the former case is more likely. Secondly, the bubble relaxation for the gas volume enclosed in a percolating chain circulating through phenocrysts and microlites, as previously described, would require timescales far greater than our dwelling times (Fig. 11, $\tau_{relax(Al+Pl)}$). Relaxation without breakup would thus leave more percolating chains after 48 h than we observe.

Despite having dwell times long enough to witness the build-up and breakup of percolating bubble chains, we do not observe gas segregation as in the experiments of Okumura et al. (2019). This is supported by the extremely long timescales, τ_{ex}, required for the gas phase migration through permeable paths (Fig. 11; Supplementary Material Text S2).

4.2. Influence of phenocrysts

No sample containing only microlites is permeable, suggesting that in our experiments, the presence of phenocrysts is perhaps necessary to foster bubble coalescence and eventual percolation. This observation needs confirmation as some extensive bubble chains are found in phenocryst-free samples (Fig. 7D).

The presence of phenocrysts in our samples has several consequences: an increase in the amount of total crystals (from ~45 vol% bulk with microlites only to ~70 vol% bulk), a reduction in interstitial space between crystals, an increased inter-bubble proximity in the residual space (between the alumina, that are most generally in direct contact with plagioclase first), and an increase in bulk viscosity, which rises by five orders of magnitude when phenocrysts are present. Such a difference between the viscosity of the melt-microlite-gas bubble mixture (Pal, 2003) and the effective viscosity with alumina (Caricchi et al., 2007; Urbain et al., 1982) gives a measure of the influence of phenocrysts. The resulting high effective viscosities due to the high crystal content suggests that alumina is immobile for the time scales explored in our experiments and constitutes, therefore, a solid framework. The enhanced proximity of bubbles in the residual space facilitates their coalescence and channelling.

At longer time scales, the relaxation of percolating chains fosters the recovery of spherical shapes. However, if the alumina framework is immobile (see the high $\tau_{relax(Al+Pl)}$ values in Fig. 11), the relaxing chains are constrained in places where alumina crystals are in near contact (samples with alumina in Fig. 5). This will eventually lead to decoalescence (or chain breakup), which can be observed mainly in the C series. It consists of the separation of previously formed permeable chains. It appears that this phenomenon happens closer to alumina crystals and that bubbles that split in this way tend to recover a larger radius of curvature, thus a more spherical shape. The dynamics of this phenomenon are deduced by interpolating comparable observations in space. In other words, we assume that a given sample contains a range of bubbles at different stages of decoalescence. Similarly, when relaxed daughter bubbles are close to regaining a spherical shape, the alumina crystals act as hindrances. This is clearly observed when comparing samples with and without alumina from the C series (Fig. 5). Without alumina, the majority of bubbles are close to spherical. Almost all these bubbles are surrounded by tangentially arranged microlites, confirming that the microlites have been displaced by bubble relaxation. In contrast, complete bubble relaxation in samples with alumina only occurs with bubbles smaller than the approximate size of the alumina grains since this relaxation only displaces the melt and microlites and, therefore, only responds to the viscosity of the melt-microlite mixture. If the bubbles are as large as the alumina crystals, relaxation depends on the much greater total viscosity. The relaxation time of the largest bubbles constrained between the alumina crystals is, therefore, much longer (up to 10^{14} s, Fig. 11) than the 48 h used here if the alumina crystals could move to accommodate the resulting large spherical bubbles.

4.3. Hierarchy of parameters controlling bubble chain formation

Reviewing the history of our samples from decompression to quench, we can classify the influence of the various processes, from coalescence to the partition of permeable chains.

During decompression, bubbles grow by exsolution of the H_2O from the melt. After decompression, there are two possible scenarios: either a bubble is close to another with only melt in between, or the bubble is surrounded by microlites. In the second case, the bubble is bound to remain small (β class), and the surrounding microlites are isolating microlites (Fig. 2A). Whether bubbles are close to one another and can coalesce is, therefore, initially linked to the random, homogeneous crystallization of microlites in the melt. Bubble proximity can be facilitated by the presence of phenocrysts because they reduce the space in which microlites crystallize and bubbles evolve.

A simple estimate of the conditions propitious to capillary displacement can be made by requiring that crystals are close enough to trap and constrain bubbles. Assuming that our tabular microlites can be approximated by oblate ellipsoids of longest axis *l* and shortest axis *a*, we

evaluate that crystals have far greater chances to form wedges when their volume fraction based on the excluded volume of an equivalent sphere of diameter l is larger than $\varphi_{RCP}\frac{a}{l}$, where $\varphi_{RCP} = 0.64$ is the random close packing of spheres. Our microlite aspect ratio $\frac{a}{l}$ being ~0.1, this estimate yields a minimum microlite volume fraction of 6.4 vol%, which is far below the 53 vol% of our experiments. Note that one would need ~60 vol% of alumina crystals to trigger capillary displacement because of their equant shapes. Capillary-induced coalescence is thus very sensitive to crystal content and shape. Conversely, bubbles should be smaller than l and not much further apart than a few bubble diameters to yield frequent encounters, which implies that the number density of bubbles should be of the same order or larger than that of the crystals. Thus, the capillary-driven coalescence we document herein is much more likely to happen with a combination of newly nucleated, small bubbles and microlites than the converse combination of older, larger bubbles only surrounded by equant phenocrysts.

If two bubbles are located next to each other, capillary forces thin the melt film, separating the two bubbles. The breakage of this film triggers coalescence. The speed of this thinning (Eq. 7) depends on several factors, such as the size of the two bubbles, the viscosity of the interstitial liquid, and the gas-melt surface tension. Some of these factors impede coalescence. Bubbles that are too large or too far apart, very high melt viscosity, or even the presence of crystals in the melt (which would increase the viscosity of the interstitial phase tenfold) would not necessarily stop coalescence but would considerably lengthen the time required for it to occur.

In our experiments, the time required for coalescence by melt thinning is of the same order as the dwelling times (Fig. 11). Two freshly coalesced bubbles yield a single prolate spheroid bubble (Fig. 10). The shape of this bubble implies variations in its surface tension forces (Fig. 2B), which are maximum at its extremities and along the recently broken inter-bubble melt film (see Fig. 10, where partially retracted inter-bubble films can be seen). These heterogeneities drive the relaxation of the bubble. This change in shape involves a displacement of the material surrounding the bubble – the melt-microlite mixture. The microlites in contact with this bubble find themselves entrained by the surface tension forces of the bubbles. If the microlite movement is decoupled from that of the melt, bubble relaxation induces creep of the interstitial melt around the microlite. Knowing that several coalesced bubbles move and evolve simultaneously, further coalescence of these bubbles is facilitated and involves ever-larger chains of bubbles. The multimodal nature of the bubble size distributions, the fact that large clusters are composed of bubble all in the 10–40 μm range of equivalent diameter with a thickness of at most 15 μm (Fig. 4), and that the pre-coalescence bubble size is in the 1–7 μm range (Fig. 3) suggests that bubble chains build locally at a similar pace and that adjacent clusters merge with each other in a staged fashion. The end result of this process is gas percolation. Being in a closed system, the absence of gas circulation within this chain prevents the connected bubbles from remaining in an elongated tortuous network because of surface tension relaxation. With time-dependent relaxation, the crystal-constrained chain breaks up into several large sub-chains of bubbles, which themselves further relax. Bubble shape variations slow down as the bubble approaches equilibrium, as surface forces weaken. Additionally, in the presence of nearby alumina crystals, bulk viscosity is such that even very large bubbles are also constrained in their relaxation. The time required for bubbles to move the alumina framework by relaxation is well beyond the times considered in this study. As a result, alumina crystals are the only obstacles to a full spherical relaxation in 48 h.

5. Implications for volcanic processes

Our experiments performed at 850 °C with various dwell times at 120 MPa best simulate the process of gas percolation in a deep (about 5 km depth using a rock density of 2400 kg/m^3), undeformed, and stagnant low-porosity (< 17 bulk vol%) crystal-rich (> 44 vol%) felsic magma. Magma column outgassing has been shown (Daffos et al., 2025; Giachetti et al., 2019; Manga et al., 1998) to occur through deformation of the bubbles during shearing of the magma as a whole, or by buoyancy if the viscosity of the magma allows it (Parmigiani et al., 2017). It has also been demonstrated that above a certain quantity of gas, outgassing is an efficient and stable phenomenon (Blower, 2001; Wright et al., 2009). Nevertheless, these gas quantities are systematically higher than those observed and theoretically present in the conduit just before an eruption (Collombet et al., 2021). One difficulty is that during an inter-eruptive period, the magma is, by definition, immobile, so that little or no material is displaced. We show here that coalescence leading to gas percolation is possible in undeformed crystal-rich magma if it contains at least 7 vol% gas. Based on crystal content and size considerations and outgassing ability, we propose three scenarios for the evolution of the gas phase in a volcano during an inter-eruptive period (Fig. 13).

The first scenario (Fig. 13A) considers an open system with gas inflow at depth and functional outgassing outlets (fracture networks, channels, and permeable gouges, Burgisser and Degruyter (2015); Christopher et al. (2015); Crozier et al. (2022); Heap et al. (2014); Rust and Cashman (2004)). In this situation, a magma composed of at least 7 vol% gas and sufficient quantities of phenocrysts and microlites is permeable at any depth. In natural systems, it is more likely that phenocrysts are inherited from the chamber and microlites have crystallized in response to strong chemical disequilibrium resulting from various events, such as decompression, magma recharge (Cashman and Blundy, 2000; Coombs et al., 2002; Laumonier et al., 2014), temperature drop due to contact with a colder host magma or host rock (Edmonds et al., 2014) or even inheritance from the chamber (Martel et al., 2006). In various magmatic contexts, similar compositions (crystal-rich with phenocrysts and/or microlites and gas-poor) resulting from a variety of different processes have been documented (Caricchi et al., 2018; Cashman and Blundy, 2000; Gardner et al., 2023; Hajimirza et al., 2021; Jones et al., 2016; Massol and Koyaguchi, 2005; McCarthy et al., 2020; Mollard et al., 2012; Mourtada-Bonnefoi and Laporte, 2002; Rutherford, 2003; Sullivan et al., 2026; Ubide et al., 2019). Although all these conditions can be met at 5 km depth, atop a magma chamber, or within a volcanic conduit, thus justifying the coexistence of phenocrysts and microlites, or even microlites alone if the magma was originally aphyric, the process presented in this study is generic and can be applied to a broader range of volcanic contexts. For example, at a shallower level in the conduit with lower pressure, given similar compositional and dynamic state of the magma, this process of shear-free permeability development at low porosity is expected to be similar. In this article is described the deepest occurrence of this process in a volcanic conduit as a starting point of outgassing that can be continued and maintained at shallower levels. Concomitantly, the value of gas permeability is predicted to increase as the magma gets to the surface because of the larger gas amount (Colombier et al., 2020; Graham et al., 2023; Klug and Cashman, 1996; Mueller et al., 2005; Parmigiani et al., 2017). Without ascent of the magma, one of the possible sources for the gas inlet is the progressive crystallization of magma in the conduit, which can lead to second boiling (Edmonds and Woods, 2018; Sisson and Bacon, 1999). In this context, second boiling is defined as a volatile phase exsolution from the melt due to oversaturation when this melt crystallizes. Such second boiling would provide gas at depth but also in the rest of the conduit (Pistone et al., 2020), therefore feeding the porous network. Another plausible mechanism of gas supply is gas flushing at depth, coming from gas exsolution of an underlying magma, most likely CO_2 fluxing (Caricchi et al., 2018; McCarthy et al., 2020; Ubide et al., 2019). In this open system, permeable networks such as those experimentally described in this study are present. We hypothesize that if gas flows through these networks, the pore pressure maintained by this flow is sufficient to keep the networks open, preventing chain collapse and/or partitioning.

The second scenario (Fig. 13B) starts with an open system like the

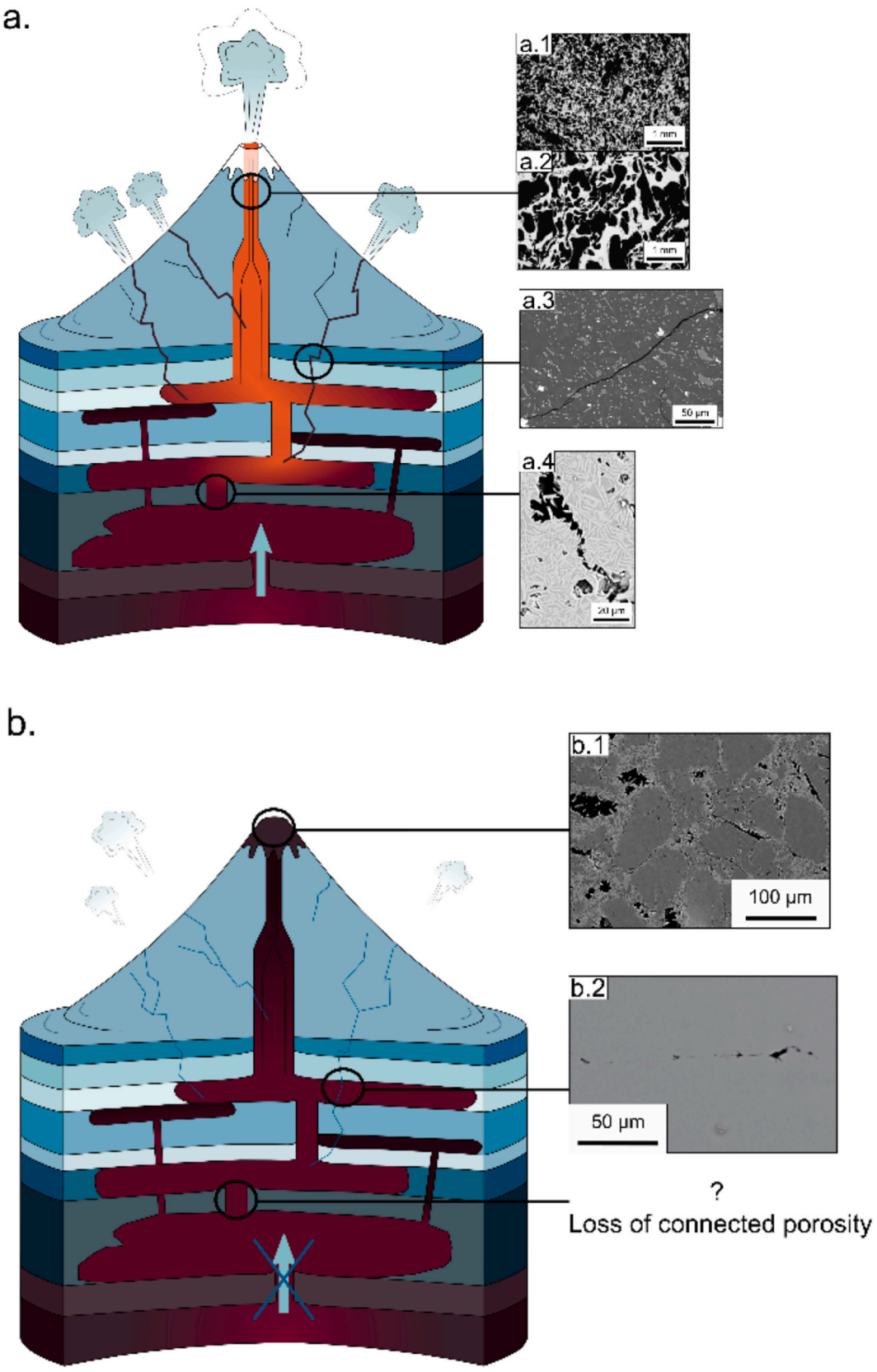

Fig. 13. Schematics of three degassing scenarios: open system, inlet off, and outlet off. The colour gradient of the magma is a relative interpretation of the activity from inactive (dark burgundy) to highly active (light orange). The blue arrow is the gas inlet, and the orange arrow is the magma inlet. Case a. describes an open system, in which deep gas is supplied and extracted from the edifice by permeable networks in the magma and fractures networks in the volcanic wall. Insets a.1 and a.2 are from Rust and Cashman (2004), a.3 is from Heap and Kennedy (2016), a.4 is sample A6 in this study. Case b represents the case where the gas inlet has stopped. As a consequence, the magma outgases via its permeable chains that eventually collapse. The remaining gas phase is strictly isolated. With time, the volcano becomes inactive. Inset b.1 is a personal unpublished sample with the same composition and manufacture conditions as in this study with the difference of having

more than 80% of crystals and less than 5% of gas, b.2 is from Lamur et al. (2019). Case c depicts a situation where all the outlets of gas at the surface are inactive (crystallized dome and healed fracture network), but an influx of new magma is coming from depth. This progressively increases the overall pressure within the volcano and eventually leads to an explosive eruption. c.1 is from Wright et al. (2009), c.2 is from Cáceres et al. (2022), c.3 is from Heap et al. (2019), c.4 is sample C4 in this study, and c.5 is sample C1 in this study.

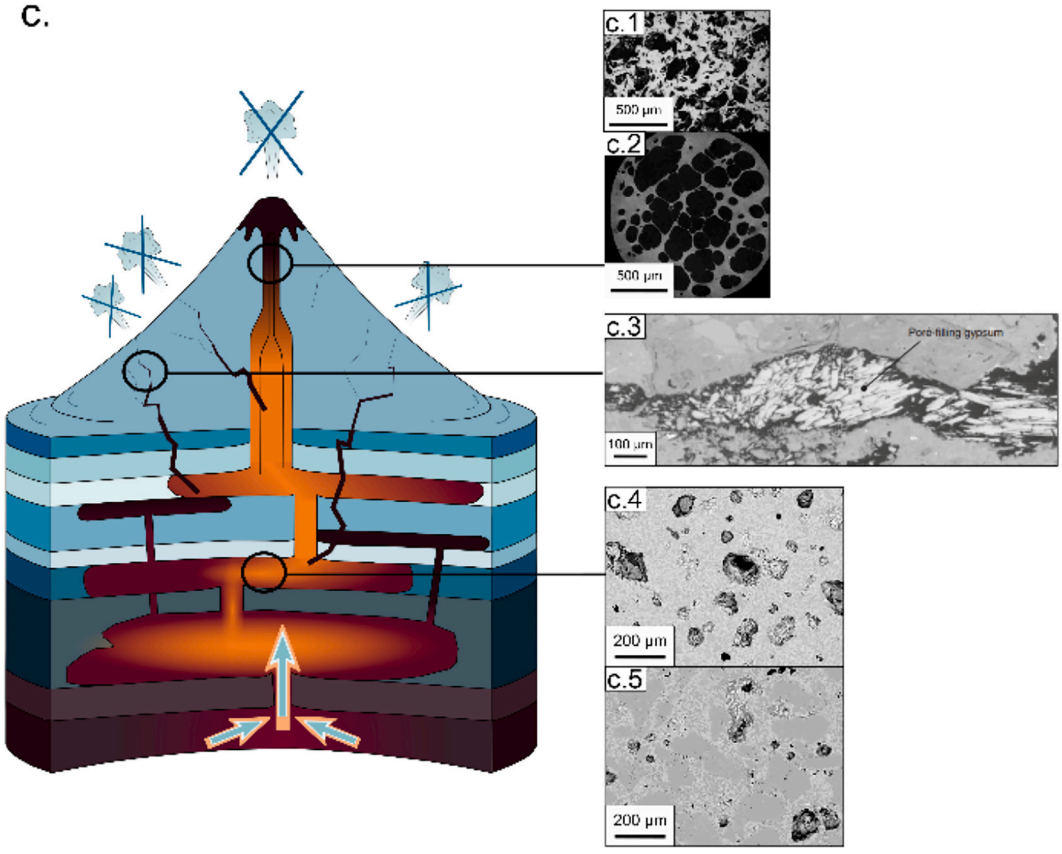

Fig. 13. (*continued*).

one described in the previous paragraph, but in which the gas inlet at depth has been cut off. The gas network would eventually empty itself through the outlet since the pressure of the gas flow through the connected porous medium is no longer sufficient to overcome the magmatic confining pressure, which will tend to close the permeable chains (melt rearrangement and chain collapse) and fracture networks (healing) (Heap et al., 2019; Lamur et al., 2019). In this case, the permeable chains would disappear, the magma would completely outgas, and only isolated porosity would remain. According to our samples, permeable chains make up approximately 10 to 50% of the total gas content (Table 2), thus leaving the outgassed magma with bulk porosity below 7 vol%. In other words, if the connected porosity is completely outgassed without recharge, the magma becomes impermeable (Bain et al., 2019; Mueller et al., 2005). In this scenario, if the inlet does not have a new influx, the volcano becomes inactive and enters a deep rest phase.

The third scenario (Fig. 13C) can be seen as a possible continuation of the second by not allowing gas outlets while reactivating gas and magma inflows from below. Stopping gas outlets may result from the formation of an impermeable dome or plug atop the magma column, in which magma massively crystallizes and fracture systems are healed (Farquharson et al., 2016; Heap et al., 2019; Wadsworth et al., 2021). In case the inlet reactivates, and an inflow of magma intrudes the resting volcano, the whole system would progressively be pressurized as no outlet (gas loss or magma extrusion) is permitted. The progression toward the surface of this magma will, therefore, rapidly come to a standstill, causing gas channelling once porosity becomes higher than 7 vol% bulk. In this case, the dynamics of the gas bubbles are identical to those highlighted in this study because, just as in our experiments, there is no outlet, so no gas flow is possible. The permeable chains will, in time, partition into large spherical bubbles (Cáceres et al., 2022), thus erasing the traces left by channelling. If the influx persists, the induced overpressure could cause the column to explode, amplified by the expansion of the isolated bubbles.

6. Conclusions

We conducted decompression experiments on synthetic magma to reproduce the percolation dynamics happening deep in a volcanic conduit. These experiments aim to constrain the sustainability of permeable gas pathways with time in the adverse conditions of gas-poor, crystal-rich, and shear-free material. We have extended the experimental work of Theurel et al. (2024), by varying the dwelling time. By concatenating the two datasets, we have a complete time series ranging from 3 min to 1 h30 to 2 days. The process documented by Theurel et al. (2024) of bubble coalescence leading to channelling, potentially generating percolation of the sample (from isolated bubble to permeable chain), has been here constrained temporally with a high level of reproducibility. This compilation of more than 20 samples allows us to clearly observe a temporal dependence of the channelling process. For short dwell times, coalescence is incomplete, and channelling is immature. For intermediate dwell time (1 h30, Theurel et al., 2024), extensive bubble chains are a dominant feature. These chains cause percolation with permeability values of $\sim 10^{-14}$ m^2 and less than 10 vol% bulk gas content. For long dwell times, we observe the breakup of permeable chains and the relaxation of the chain remnants into spherical shapes. The scarce presence of permeable samples at short and long dwell times

shows that in a closed system, channelling and percolation patterns are dynamic and somewhat ephemeral.

We use the timescales of several processes to quantify the phenomena expected to arise during percolation, from the viscous relaxation of bubbles in response to decompression and the subsequent formation of permeable bubble chains by coalescence to the relaxation of the permeable network that leads to samples once again impermeable. First, we quantify bubble growth time with respect to dynamic viscosity, as described in Okumura et al. (2019). We find that this timescale is systematically shorter than the shortest dwell time explored in this study, implying that all spherical bubbles observed in our samples are at mechanical equilibrium. If bubble growth happens in a wedge made by two adjacent microlites, the constricted bubble migrates away from the wedge because of uneven surface tension distribution. This phenomenon triggers a displacement described by the model of Reyssat (2014). This model yields the distance the bubble can travel if it is not disturbed by any obstacle on its trajectory. In our experiments, calculations suggest that bubbles have traveled by up to twice their size before the shortest dwell time. We identify this phenomenon as the main driving force for primary bubble displacement, fostering bubble proximity with one another. We then calculate the timescale of melt film rupture leading to bubble coalescence following Castro et al. (2012a) and Giachetti et al. (2019). The fastest coalescence is completed within around 6 min for the smallest (~2 μm equivalent diameter) bubbles, whereas the slowest coalescence happens within 30 h for the largest bubbles (δ class, >300 μm equivalent diameter), which is still within the timescales explored in this study. These results are consistent with our observations; a 3-min dwell time is generally too short for extensive coalescence to occur, leading to immature channelling and overall impermeability of the samples. Finally, using Okumura et al. (2012), we calculated bubble relaxation timescales and noted that most of the estimates were far above the timescales explored in this study, ranging from 20 s for the smallest bubbles to more than 10^{13} s for the largest channels. This seemed paradoxical because we observed channel relaxation in our samples. The reason is that while the relaxation process is underway, other phenomena occur, such as the constriction by an effectively immobile phenocryst framework, which ultimately leads to the breakup of bubble chains. Thus, the timescale required to reach a fully relaxed shape decreases over time because of breakup. As we do not have a time resolution for the breakup process occurring between 1 h30 and 48 h, the Okumura et al. (2012) timescale gives a first-order quantification that overestimates the actual duration of that phenomenon.

In summary, this study shows that the bubble coalescence that leads to channelling and percolation at low gas volume fraction is caused by capillary migration of confined bubbles that could not maintain a spherical shape because they grew surrounded (and constrained) by microlites. It also shows that while the presence of phenocrysts is perhaps essential for the development of permeable chains, they can also be the cause of percolating chain partitioning, which makes low-porosity permeability ephemeral in closed systems.

CRediT author statement

Anna Theurel: Conceptualization, Methodology, Formal analysis, Investigation, Data Curation, Writing – Original Draft, Writing - Review & Editing, Visualization, Funding acquisition.

Marielle Collombet: Conceptualization, Methodology, Validation, Formal analysis, Investigation, Resources, Data Curation, Writing - Review & Editing, Visualization, Supervision, Project administration, Funding acquisition.

Alain Burgisser: Conceptualization, Methodology, Validation, Formal analysis, Investigation, Resources, Data Curation, Writing - Review & Editing, Visualization, Supervision, Project administration, Funding acquisition.

Caroline Martel: Conceptualization, Methodology, Validation, Investigation, Resources, Writing - Review & Editing, Supervision, Project administration.

Laurent Arbaret: Methodology, Resources, Funding acquisition.

Rémi Champallier: Resources.

CRediT authorship contribution statement

Anna Theurel: Writing – review & editing, Writing – original draft, Visualization, Methodology, Investigation, Funding acquisition, Formal analysis, Data curation, Conceptualization. **Marielle Collombet:** Writing – review & editing, Validation, Supervision, Software, Resources, Project administration, Methodology, Investigation, Funding acquisition, Formal analysis, Conceptualization. **Alain Burgisser:** Writing – review & editing, Validation, Supervision, Software, Resources, Project administration, Methodology, Investigation, Funding acquisition, Formal analysis, Conceptualization. **Caroline Martel:** Writing – review & editing, Validation, Supervision, Resources, Project administration, Methodology, Investigation, Funding acquisition, Conceptualization. **Laurent Arbaret:** Writing – review & editing, Visualization, Software, Resources. **Rémi Champallier:** Resources.

Declaration of competing interest

The authors declare that they have no known competing financial interests or personal relationships that could have appeared to influence the work reported in this paper.

Acknowledgements

This study is partially supported by the Agence Nationale pour la Recherche MECAMUSH (ANR-19-CE31-0007). This work is part of A. Theurel PhD thesis supported by French national Grant from the Ministère de l'Enseignement Superieur, de la Recherche et de l'Innovation. The computations presented in this paper were performed using the GRICAD infrastructure (gricad.univ-grenoble-alpes.fr), which is supported by Grenoble research communities and μCT devices are supported by the LABEX VOLTAIRE project (ANR-10-LABX-100-01). The authors thank the reviewers and the editor for the constructive comments that helped improve this manuscript.

Appendix A. Supplementary data

Supplementary data to this article can be found online at https://doi.org/10.1016/j.jvolgeores.2026.108612.

Data availability

Complete Dataset is available in the SI

References

Bagdassarov, N., Dorfman, A., Dingwell, D.B., 2000. Effect of alkalis, phosphorus, and water on the surface tension of haplogranite melt. Am. Mineral. 85, 33–40. https://doi.org/10.2138/am-2000-0105.

Bain, A.A., Lamur, A., Kendrick, J.E., Lavallée, Y., Calder, E.S., Cortés, J.A., Butler, I.B., Cortés, G.P., 2019. Constraints on the porosity, permeability and porous microstructure of highly-crystalline andesitic magma during plug formation. J. Volcanol. Geotherm. Res. 379, 72–89. https://doi.org/10.1016/j.jvolgeores.2019.05.001.

Blower, J.D., 2001. Factors controlling permeability-porosity relationships in magma. Bull. Volcanol. 63, 497–504. https://doi.org/10.1007/s004450100172.

Bretagne, E., Wadsworth, F.B., Vasseur, J., Humphreys, M.C.S., Dingwell, D.B., Dobson, K.J., Mangler, M.F., Rooyakkers, S.M., 2023. The permeability of loose magma mush. Geology 51, 829–832. https://doi.org/10.1130/G51133.1.

Burgisser, A., Degruyter, W., 2015. Magma ascent and degassing at shallow levels. In: The Encyclopedia of Volcanoes. Elsevier, pp. 225–236. https://doi.org/10.1016/B978-0-12-385938-9.00011-0.

Burgisser, A., Bechon, T., Chevalier, L., Collombet, M., Arbaret, L., Forien, M., 2019. Conduit processes during the February 11, 2010 Vulcanian eruption of Soufrière Hills, Montserrat. J. Volcanol. Geotherm. Res. 373, 23–35. https://doi.org/10.1016/j.jvolgeores.2019.01.020.

Cáceres, F., Scheu, B., Colombier, M., Hess, K.-U., Feisel, Y., Ruthensteiner, B., Dingwell, D.B., 2022. The roles of microlites and phenocrysts during degassing of

silicic magma. Earth Planet. Sci. Lett. 577, 117264. https://doi.org/10.1016/j.epsl.2021.117264.
Caricchi, L., Burlini, L., Ulmer, P., Gerya, T., Vassalli, M., Papale, P., 2007. Non-Newtonian rheology of crystal-bearing magmas and implications for magma ascent dynamics. Earth Planet. Sci. Lett. 264, 402–419. https://doi.org/10.1016/j.epsl.2007.09.032.
Caricchi, L., Sheldrake, T.E., Blundy, J., 2018. Modulation of magmatic processes by CO2 flushing. Earth Planet. Sci. Lett. 491, 160–171. https://doi.org/10.1016/j.epsl.2018.03.042.
Caricchi, L., Montagna, C.P., Aiuppa, A., Lages, J., Tamburello, G., Papale, P., 2024. CO_2 flushing triggers paroxysmal eruptions at open conduit basaltic volcanoes. JGR Solid Earth 129, e2023JB028486. https://doi.org/10.1029/2023JB028486.
Cashman, K., Blundy, J., 2000. Degassing and crystallization of ascending andesite and dacite. Philosophical transactions of the Royal Society of London. Ser. A Math. Phys. Eng. Sci. 358, 1487–1513. https://doi.org/10.1098/rsta.2000.0600.
Castro, J.M., Burgisser, A., Schipper, C.I., Mancini, S., 2012. Mechanisms of bubble coalescence in silicic magmas. Bull. Volcanol. 74, 2339–2352. https://doi.org/10.1007/s00445-012-0666-1.
Cheng, H.C., Lemlich, R., 1983. Errors in the measurement of bubble size distribution in foam. Ind. Eng. Chem. Fundam. 22, 105–109. https://doi.org/10.1021/i100009a018.
Christopher, T.E., Blundy, J., Cashman, K., Cole, P., Edmonds, M., Smith, P.J., Sparks, R. S.J., Stinton, A., 2015. Crustal-scale degassing due to magma system destabilization and magma-gas decoupling at Soufrière Hills Volcano, Montserrat. Geochem. Geophys. Geosyst. 16, 2797–2811. https://doi.org/10.1002/2015GC005791.
Collombet, M., Burgisser, A., Colombier, M., Gaunt, E., 2021. Evidence for deep gas loss in open volcanic systems. Bull. Volcanol. 83, 7. https://doi.org/10.1007/s00445-020-01433-0.
Colombier, M., Wadsworth, F.B., Scheu, B., Vasseur, J., Dobson, K.J., Cáceres, F., Allabar, A., Marone, F., Schlepütz, C.M., Dingwell, D.B., 2020. In situ observation of the percolation threshold in multiphase magma analogues. Bull. Volcanol. 82, 32. https://doi.org/10.1007/s00445-020-1370-1.
Coombs, M.L., Eichelberger, J.C., Rutherford, M.J., 2002. Experimental and textural constraints on ma¢c enclave formation in volcanic rocks. J. Volcanol. Geotherm. Res. 119, 125–144.
Crozier, J., Tramontano, S., Forte, P., Oliva, S.J.C., Gonnermann, H.M., Lev, E., Manga, M., Myers, M., Rader, E., Ruprecht, P., Tuffen, H., Paisley, R., Houghton, B. F., Shea, T., Schipper, C.I., Castro, J.M., 2022. Outgassing through magmatic fractures enables effusive eruption of silicic magma. J. Volcanol. Geotherm. Res. 430, 107617. https://doi.org/10.1016/j.jvolgeores.2022.107617.
Daffos, C., Martel, C., Arbaret, L., Champallier, R., 2025. Bubble connectivity in experimentally-sheared crystal-bearing silicic melts. C. R. Géosci. 356, 53–70. https://doi.org/10.5802/crgeos.214.
deGraffenried, R.L., Larsen, J.F., Graham, N.A., Cashman, K.V., 2019. The influence of phenocrysts on degassing in crystal-bearing magmas with rhyolitic groundmass melts. Geophys. Res. Lett. 46, 5127–5136. https://doi.org/10.1029/2018GL081822.
Degruyter, W., Parmigiani, A., Huber, C., Bachmann, O., 2019. How do volatiles escape their shallow magmatic hearth? Phil. Trans. R. Soc. A 377, 20180017. https://doi.org/10.1098/rsta.2018.0017.
Edmonds, M., Woods, A.W., 2018. Exsolved volatiles in magma reservoirs. J. Volcanol. Geotherm. Res. 368, 13–30. https://doi.org/10.1016/j.jvolgeores.2018.10.018.
Edmonds, M., Humphreys, M.C.S., Hauri, E.H., Herd, R.A., Wadge, G., Rawson, H., Ledden, R., Plail, M., Barclay, J., Aiuppa, A., Christopher, T.E., Giudice, G., Guida, R., 2014. Chapter 16 Pre-eruptive vapour and its role in controlling eruption style and longevity at Soufrière Hills Volcano. Memoirs 39, 291–315. https://doi.org/10.1144/M39.16.
Farquharson, J.I., Heap, M.J., Lavallée, Y., Varley, N.R., Baud, P., 2016. Evidence for the development of permeability anisotropy in lava domes and volcanic conduits. J. Volcanol. Geotherm. Res. 323, 163–185. https://doi.org/10.1016/j.jvolgeores.2016.05.007.
Gardner, J.E., Ketcham, R.A., Moore, G., 2013. Surface tension of hydrous silicate melts: constraints on the impact of melt composition. J. Volcanol. Geotherm. Res. 267, 68–74. https://doi.org/10.1016/j.jvolgeores.2013.09.007.
Gardner, J.E., Wadsworth, F.B., Carley, T.L., Llewellin, E.W., Kusumaatmaja, H., Sahagian, D., 2023. Bubble formation in Magma. Annu. Rev. Earth Planet. Sci. 51, 131–154. https://doi.org/10.1146/annurev-earth-031621-080308.
Giachetti, T., Druitt, T.H., Burgisser, A., Arbaret, L., Galven, C., 2010. Bubble nucleation, growth and coalescence during the 1997 Vulcanian explosions of Soufrière Hills Volcano, Montserrat. J. Volcanol. Geotherm. Res. 193, 215–231.
Giachetti, T., Gonnermann, H.M., Gardner, J.E., Burgisser, A., Hajimirza, S., Earley, T.C., Truong, N., Toledo, P., 2019. Bubble coalescence and percolation threshold in expanding rhyolitic Magma. Geochem. Geophys. Geosyst. 20, 1054–1074. https://doi.org/10.1029/2018GC008006.
Graham, N.A., Larsen, J.F., Tasa, K.Y., deGraffenried, R.L., Cashman, K.V., McCartney, K. N., 2023. Controls of crystal shape on degassing mechanisms in crystal-rich magmas with rhyolitic groundmass melts. Earth Planet. Sci. Lett. 601, 117891. https://doi.org/10.1016/j.epsl.2022.117891.
Hajimirza, S., Gonnermann, H.M., Gardner, J.E., 2021. Reconciling bubble nucleation in explosive eruptions with geospeedometers. Nat. Commun. 12, 283. https://doi.org/10.1038/s41467-020-20541-1.
Heap, M.J., Kennedy, B.M., 2016. Exploring the scale-dependent permeability of fractured andesite. Earth Planet. Sci. Lett. 447, 139–150. https://doi.org/10.1016/j.epsl.2016.05.004.
Heap, M.J., Lavallée, Y., Petrakova, L., Baud, P., Reuschlé, T., Varley, N.R., Dingwell, D. B., 2014. Microstructural controls on the physical and mechanical properties of edifice-forming andesites at Volcán de Colima, Mexico. JGR Solid Earth 119, 2925–2963. https://doi.org/10.1002/2013JB010521.
Heap, M.J., Tuffen, H., Wadsworth, F.B., Reuschlé, T., Castro, J.M., Schipper, C.I., 2019. The permeability evolution of Tuffisites and implications for outgassing through dense rhyolitic Magma. JGR Solid Earth 124, 8281–8299. https://doi.org/10.1029/2018JB017035.
Hess, K.-U., Dingwell, D.D., 1996. Viscosities of hydrous leucogranitic melts: a non-Arrhenian model. Am. Mineral. 81, 1297–1300.
Jaupart, C., Allègre, C.J., 1991. Gas content, eruption rate and instabilities of eruption regime in silicic volcanoes. Earth Planet. Sci. Lett. 102, 413–429. https://doi.org/10.1016/0012-821X(91)90032-D.
Jones, T.J., McNamara, K., Eychenne, J., Rust, A.C., Cashman, K.V., Scheu, B., Edwards, R., 2016. Primary and secondary fragmentation of crystal-bearing intermediate magma. J. Volcanol. Geotherm. Res. 327, 70–83. https://doi.org/10.1016/j.jvolgeores.2016.06.022.
Ketcham, R.A., 2005. Computational methods for quantitative analysis of three-dimensional features in geological specimens. Geosphere 1, 32–41.
Klug, C., Cashman, K.V., 1996. Permeability development in vesiculating magmas: implications for fragmentation. Bull. Volcanol. 58, 87–100. https://doi.org/10.1007/s004450050128.
Lamur, A., Kendrick, J.E., Wadsworth, F.B., Lavallée, Y., 2019. Fracture healing and strength recovery in magmatic liquids. Geology 47, 195–198. https://doi.org/10.1130/G45512.1.
Larsen, J.F., Gardner, J.E., 2000. Experimental constraints on bubble interactions in rhyolite melts: implications for vesicle size distributions. Earth Planet. Sci. Lett. 180, 201–214. https://doi.org/10.1016/S0012-821X(00)00166-7.
Laumonier, M., 2013. Mélange de Magmas à HP-HT, Contraintes Expérimentales et Application au Magmatisme d'arc. Univeriste d'Orleans.
Laumonier, M., Scaillet, B., Pichavant, M., Champallier, R., Andujar, J., Arbaret, L., 2014. On the conditions of magma mixing and its bearing on andesite production in the crust. Nat. Commun. 5, 5607. https://doi.org/10.1038/ncomms6607.
Launeau, P., 2004. Evidence of magmatic flow by 2-D image analysis of 3-D shape preferred orientation distributions. Bull. Soc. Géol. Fr. 175, 331–350. https://doi.org/10.2113/175.4.331.
Lindoo, A., Larsen, J.F., Cashman, K.V., Dunn, A.L., Neill, O.K., 2016. An experimental study of permeability development as a function of crystal-free melt viscosity. Earth Planet. Sci. Lett. 435, 45–54. https://doi.org/10.1016/j.epsl.2015.11.035.
Lindoo, A., Larsen, J.F., Cashman, K.V., Oppenheimer, J., 2017. Crystal controls on permeability development and degassing in basaltic andesite magma. Geology 45, 831–834. https://doi.org/10.1130/G39157.1.
Manga, M., Castro, J., Cashman, K.V., Loewenberg, M., 1998. Rheology of bubble-bearing magmas. J. Volcanol. Geotherm. Res. 84, 15–28.
Martel, C., 2012. Eruption dynamics inferred from microlite crystallization experiments: application to Plinian and dome-forming eruptions of Mt. Pelee (Martinique, Lesser Antilles). J. Petrol. 53, 699–725. https://doi.org/10.1093/petrology/egr076.
Martel, C., Radadi Ali, A., Poussineau, S., Gourgaud, A., Pichavant, M., 2006. Basalt-inherited microlites in silicic magmas: evidence from Mount Pelée (Martinique, French West Indies). Geol 34, 905. https://doi.org/10.1130/G22672A.1.
Massol, H., Koyaguchi, T., 2005. The effect of magma flow on nucleation of gas bubbles in a volcanic conduit. J. Volcanol. Geotherm. Res. 143, 69–88. https://doi.org/10.1016/j.jvolgeores.2004.09.011.
McCarthy, A., Chelle-Michou, C., Blundy, J.D., Vonlanthen, P., Meibom, A., Escrig, S., 2020. Taking the pulse of volcanic eruptions using plagioclase glomerocrysts. Earth Planet. Sci. Lett. 552, 116596. https://doi.org/10.1016/j.epsl.2020.116596.
Mollard, E., Martel, C., Bourdier, J.-L., 2012. Decompression-induced crystallization in hydrated silica-rich melts: empirical models of experimental plagioclase nucleation and growth kinetics. J. Petrol. 53, 1743–1766. https://doi.org/10.1093/petrology/egs031.
Morgan, Dan J., Jerram, Dougal A., 2006. On estimating crystal shape for crystal size distribution analysis. J. Volcanol. Geotherm. Res. 154 (1–2), 1–7. https://doi.org/10.1016/j.jvolgeores.2005.09.016. ISSN 0377-0273. https://www.sciencedirect.com/science/article/pii/S0377027306000382.
Mourtada-Bonnefoi, C.C., Laporte, D., 2002. Homogeneous bubble nucleation in rhyolitic magmas: an experimental study of the effect of H_2 O and CO_2. J. Geophys. Res. 107. https://doi.org/10.1029/2001JB000290.
Moussallam, Y., Peters, N., Masias, P., Apaza, F., Barnie, T., Ian Schipper, C., Curtis, A., Tamburello, G., Aiuppa, A., Bani, P., Giudice, G., Pieri, D., Davies, A.G., Oppenheimer, C., 2017. Magmatic gas percolation through the old lava dome of El Misti volcano. Bull. Volcanol. 79, 46. https://doi.org/10.1007/s00445-017-1129-5.
Mueller, S., Melnik, O., Spieler, O., Scheu, B., Dingwell, D.B., 2005. Permeability and degassing of dome lavas undergoing rapid decompression: an experimental determination. Bull. Volcanol. 67, 526–538. https://doi.org/10.1007/s00445-004-0392-4.
Mueller, S., Scheu, B., Spieler, O., Dingwell, D.B., 2008. Permeability control on magma fragmentation. Geol 36, 399. https://doi.org/10.1130/G24605A.1.
Nguyen, C.T., Gonnermann, H.M., Chen, Y., Huber, C., Maiorano, A.A., Gouldstone, A., Dufek, J., 2013. Film drainage and the lifetime of bubbles. Geochem. Geophys. Geosyst. 14, 3616–3631. https://doi.org/10.1002/ggge.20198.
Nowak, M., Behrens, H., 1997. An experimental investigation on diffusion of water in haplogranitic melts. Contrib. Mineral. Petrol. 126, 365–376. https://doi.org/10.1007/s004100050256.
Okumura, S., Nakamura, M., Tsuchiyama, A., Nakano, T., Uesugi, K., 2008. Evolution of bubble microstructure in sheared rhyolite: formation of a channel-like bubble network. J. Geophys. Res. 113, 2007JB005362. https://doi.org/10.1029/2007JB005362.

Okumura, S., Nakamura, M., Nakano, T., Uesugi, K., Tsuchiyama, A., 2012. Experimental constraints on permeable gas transport in crystalline silicic magmas. Contrib. Mineral. Petrol. 164, 493–504. https://doi.org/10.1007/s00410-012-0750-8.

Okumura, S., De Silva, L., Nakamura, M., Sasaki, O., 2019. Caldera-forming eruptions of mushy magma modulated by feedbacks between ascent rate, gas retention/loss and bubble/crystal framework interaction. Sci. Rep. 9, 15845. https://doi.org/10.1038/s41598-019-52272-9.

Oppenheimer, J., Rust, A.C., Cashman, K.V., Sandnes, B., 2015. Gas migration regimes and outgassing in particle-rich suspensions. Front. Phys. 3. https://doi.org/10.3389/fphy.2015.00060.

Pal, R., 2003. Rheological behavior of bubble-bearing magmas. Earth Planet. Sci. Lett. 207, 165–179. https://doi.org/10.1016/S0012-821X(02)01104-4.

Parmigiani, A., Degruyter, W., Leclaire, S., Huber, C., Bachmann, O., 2017. The mechanics of shallow magma reservoir outgassing. Geochem. Geophys. Geosyst. 18, 2887–2905. https://doi.org/10.1002/2017GC006912.

Pistone, M., Caricchi, L., Ulmer, P., Burlini, L., Ardia, P., Reusser, E., Marone, F., Arbaret, L., 2012. Deformation experiments of bubble- and crystal-bearing magmas: rheological and microstructural analysis. J. Geophys. Res. 117, 2011JB008986. https://doi.org/10.1029/2011JB008986.

Pistone, M., Baumgartner, L.P., Bégué, F., Jarvis, P.A., Bloch, E., Robyr, M., Müntener, O., Sisson, T.W., Blundy, J.D., 2020. Felsic melt and gas mobilization during magma solidification: an experimental study at 1.1 kbar. Front. Earth Sci. 8, 175. https://doi.org/10.3389/feart.2020.00175.

Reyssat, E., 2014. Drops and bubbles in wedges. J. Fluid Mech. 748, 641–662. https://doi.org/10.1017/jfm.2014.201.

Rust, A.C., Cashman, K.V., 2004. Permeability of vesicular silicic magma: inertial and hysteresis effects. Earth Planet. Sci. Lett. 228, 93–107. https://doi.org/10.1016/j.epsl.2004.09.025.

Rutherford, M.J., 2003. Magmatic conditions and magma ascent as indicated by hornblende phase equilibria and reactions in the 1995-2002 Soufriere Hills Magma. J. Petrol. 44, 1433–1453. https://doi.org/10.1093/petrology/44.8.1433.

Saar, M.O., Manga, M., 1999. Permeability-porosity relationship in vesicular basalts. Geophys. Res. Lett. 26, 111–114. https://doi.org/10.1029/1998GL900256.

Sahagian, D.L., Proussevitch, A.A., 1998. 3D particle size distributions from 2D observations: stereology for natural applications. J. Volcanol. Geotherm. Res. 84, 173–196.

Sisson, T.W., Bacon, C.R., 1999. Gas-driven filter pressing in magmas. Geol 27, 613. https://doi.org/10.1130/0091-7613(1999)027%253C0613:GDFPIM%253E2.3.CO;2.

Sullivan, P., Llewellin, E.W., Wadsworth, F.B., Colucci, S., Kusumaatmaja, H., 2026. The nucleation and growth of mixed H2O–CO2 bubbles in magmas. J. Volcanol. Geotherm. Res. 472, 108538. https://doi.org/10.1016/j.jvolgeores.2026.108538.

Theurel, A., Collombet, M., Burgisser, A., Martel, C., Arbaret, L., Champallier, R., 2024. Experimental evidence of primary permeability at very low gas content in crystal-rich Silicic Magma. Geophys. Res. Lett. 51, e2024GL108389. https://doi.org/10.1029/2024GL108389.

Ubide, T., Caulfield, J., Brandt, C., Bussweiler, Y., Mollo, S., Di Stefano, F., Nazzari, M., Scarlato, P., 2019. Deep magma storage revealed by multi-method elemental mapping of clinopyroxene Megacrysts at Stromboli volcano. Front. Earth Sci. 7, 239. https://doi.org/10.3389/feart.2019.00239.

Urbain, G., Bottinga, Y., Richet, P., 1982. Viscosity of liquid silica, silicates and alumino-silicates. Geochim. Cosmochim. Acta 46, 1061–1072. https://doi.org/10.1016/0016-7037(82)90059-X.

Wadsworth, F.B., Vasseur, J., Llewellin, E.W., Brown, R.J., Tuffen, H., Gardner, J.E., Kendrick, J.E., Lavallée, Y., Dobson, K.J., Heap, M.J., Dingwell, D.B., Hess, K.-U., Schauroth, J., Von Aulock, F.W., Kushnir, A.R.L., Marone, F., 2021. A model for permeability evolution during volcanic welding. J. Volcanol. Geotherm. Res. 409, 107118. https://doi.org/10.1016/j.jvolgeores.2020.107118.

Wright, H.M.N., Cashman, K.V., Rosi, M., Cioni, R., 2006a. Breadcrust bombs as indicators of Vulcanian eruption dynamics at Guagua Pichincha volcano, Ecuador. Bull. Volcanol. 69, 281–300. https://doi.org/10.1007/s00445-006-0073-6.

Wright, H.M.N., Roberts, J.J., Cashman, K.V., 2006b. Permeability of anisotropic tube pumice: Model calculations and measurements. Geophys. Res. Lett. 33, 2006GL027224. https://doi.org/10.1029/2006GL027224.

Wright, H.M.N., Cashman, K.V., Gottesfeld, E.H., Roberts, J.J., 2009. Pore structure of volcanic clasts: Measurements of permeability and electrical conductivity. Earth Planet. Sci. Lett. 280, 93–104. https://doi.org/10.1016/j.epsl.2009.01.023.

Yokoyama, T., Takeuchi, S., 2009. Porosimetry of vesicular volcanic products by a water-expulsion method and the relationship of pore characteristics to permeability. J. Geophys. Res. 114, 2008JB005758. https://doi.org/10.1029/2008JB005758.